ROYAL SOCIETY OF CHEMISTRY

PAPER

Check for updates

Elucidating the detrimental effect of intercalated protons in Ni-rich NCMs on structural stability and cycle life

Rebecca Wilhelm, [ID] * Simon Helmer, [ID] Hubert A. Gasteiger [ID] and Stefan Oswald [ID] *†

Ni-rich NCMs are widely used as commercial cathode active materials for high-energy lithium-ion batteries due to their high specific capacity. However, upon exposure to liquid or gaseous water or protons from other sources, these materials are prone to cation-exchange reactions, in which lithium ions in the near-surface region of the NCM particles are replaced by protons. To investigate the impact of the protonation on electrochemical performance, controlled amounts of protons were introduced deliberately into NCM831205 ($LiNi_{0.83}Co_{0.12}Mn_{0.05}O_2$) through a washing process. On-line electrochemical mass spectrometry (OEMS) revealed that the protons can be deintercalated at high voltages exceeding 4.5 V_{Li}, while X-ray photoelectron spectroscopy (XPS) showed their gradual removal during extended cycling even at low upper cutoff potentials. As protons are removed —at least in part— as water, an oxygen-depleted surface layer forms. As confirmed by electrochemical impedance spectroscopy (EIS), this degraded surface gives rise to a detrimental charge-transfer resistance, thereby compromising both rate capability and long-term capacity retention. This newly identified, proton-induced degradation pathway underscores the importance of optimized dry processing and storage conditions to mitigate performance losses and extend the cycle life of layered-oxide-based lithium-ion batteries.

Broader context

Li-ion batteries are a crucial technology to decarbonize transportation and contribute to a greener future. To achieve, *e.g.*, the necessary driving ranges of electric vehicles, high-energy materials such as layered lithium transition-metal oxides (NCMs) are commercially established cathode active materials. However, the processing of Ni-rich NCMs on an industrial scale is challenging since the washing after synthesis, improper storage, and/or aqueous slurry mixing introduces protons into the NCM structure, which partially replace the lithium ions. Within this study, we discover a novel, proton-driven degradation mechanism by investigating a state-of-the-art NCM material with controlled amounts of deliberately introduced protons. We find that intercalated protons decrease rate capability while, upon extended charge/discharge cycling, the protons deintercalate, form an oxygen-depleted, highly resistive layer at the surface of the NCM, and decompose the $LiPF_6$ conductive salt in the electrolyte. Overall, protons present in the NCM destabilize its structure, which then degrades during battery operation, limiting the lifetime of NCM-based battery cells drastically. Therefore, proper storage and handling of NCMs is crucial.

Introduction

Owing to their high specific capacity and energy density, Ni-rich layered lithium transition-metal (TM) oxides (NCMs, *i.e.*, $LiMO_2$ with M = Ni, Co, Mn or $LiNi_aCo_bMn_cO_2$ with $a + b + c = 1$) are state-of-the-art cathode active materials (CAMs) in lithium-ion batteries (LIBs) for the use in high-energy applications, such as electric vehicles.[1–4] While they exhibit a high theoretical specific capacity of 275 mAh g_{NCM}^{-1}, high degrees of delithiation induce the release of lattice oxygen, which is accompanied by a phase change from the layered to a rock-salt structure in the near-surface region of the NCM particles.[5,6] Thus, the practical capacity needs to be limited to ~85% of the full state-of-charge (SOC) window.[5–9] At higher SOCs, the release of lattice oxygen increases resistance[6,7,10–12] and triggers side reactions with the electrolyte.[13–17]

In contrast to low-/mid-nickel NCMs, a higher nickel content leads to a highly reactive surface,[18,19] necessitating that Ni-rich materials are handled, stored, and processed under dry conditions.[20,21] Improper material handling leads to a rapid decline of capacity retention and an increased

Technical University of Munich, TUM School of Natural Sciences, Department of Chemistry and Catalysis Research Center, Chair of Technical Electrochemistry, Lichtenbergstraße 4, 85748 Garching, Germany. E-mail: Rebecca.Wilhelm@tum.de, Stefan.Oswald@tum.de
†Current affiliation: Yusuf Hamied Department of Chemistry, University of Cambridge, Cambridge, UK.

impedance build-up,[19,22] that is generally attributed to the formation of surface contaminants, such as hydroxides and carbonates.[19,22–25] These unwanted species may react with the electrolyte components, which, in combination with the decomposition of the contaminants, leads to unwanted gassing and side reactions during battery operation.[12,19,26–28] Interestingly, in addition to the formation of surface species, it was shown that ambient storage in a humid environment leads to a so-called lithium/proton (Li^+/H^+) ion exchange,[23,25,29] where protons intercalate into the near-surface region of the NCM particles, forming a partially protonated/lithiated NCM (denoted as $H_xLi_xMO_2$), comprising a fully protonated shell (HMO_2) and a fully lithiated core ($LiMO_2$), while the replaced Li^+ forms LiOH in solution:[30–33]

$$LiMO_2 + H_2O \rightarrow H_xLi_{1-x}MO_2 + LiOH \quad (1)$$
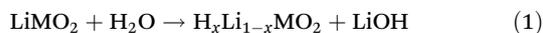
While CAMs stored under humid environments were found to perform significantly worse than a properly stored CAM,[23,29] it has been unclear whether the surface contaminants or the protons are (more) detrimental for the cell performance. In related studies, where the ion exchange was induced through washing with water, a compromised capacity retention, decreased rate capability, and impedance build-up was observed,[22,34–38] hinting towards a proton-driven degradation instead of one related to the surface contaminants; however, the underlying degradation mechanism has not yet been identified. Therefore, it is the goal of this study to isolate the impact of the protons on the electrochemical performance from the one of the surface contaminants, elucidating their role in the observed performance deterioration.

To provide well-characterized protonated materials, in the first part of this study, a Ni-rich NCM with a nickel content of 83 mol% was investigated. This material is both of highest commercial relevance and also prone to interact with water; yet, it does not suffer from the same intrinsic structural instability at high SOCs as a nickel-only material (i.e., $LiNiO_2$).[39] The NCM was then washed with varying parameters, and not only were the amounts of protons quantified using five independent techniques, but the material was also thoroughly characterized regarding structural changes after washing.[32] From this previous study, two active materials with 1 and 2 mol% of protons were obtained and here characterized in electrochemical experiments. This approach does not only allow us to understand how the presence of protons affects the electrochemistry but also to identify and quantify the parasitic reactions and degradation modes caused by protons. First, we will show at which potential the protons are removed from the NCM electrochemically using on-line electrochemical mass spectrometry (OEMS). Furthermore, the effect of protons on the NCM potential curve during the first charge as well as on their cycle life and resistance growth during extended half-/full-cell testing is investigated. Lastly, a reaction pathway will be formulated for this novel, proton-driven degradation mode, where the electrochemical cycling data is supported

by electrochemical impedance spectroscopy (EIS), elemental analysis, and X-ray photoelectron spectroscopy (XPS).

Materials & methods

Material and electrode preparation

In this study, the effect of washing on Ni-rich NCMs is to be investigated. For this, uncoated and untreated NCM831205 ($LiNi_{0.83}Co_{0.12}Mn_{0.05}O_2$, 0.62 m^2_{BET} g_{NCM}^{-1}, undisclosed commercial supplier, labeled "NCM-prist") was used and compared to its protonated derivatives. The latter were prepared by stirring 5 g of NCM-prist at 500 rpm under argon in degassed, deionized water at room temperature for 1 h. Following the procedure described in our previous study,[32] where the proton content in the same material after washing was quantified using various methods, such as titration, PGAA, TGA-MS, XRD, and XPS, washing with a water-to-CAM ratio of 1 : 1 w/w for 1 h results in a proton content of approx. 1 mol%, equivalent to $H_{0.01}Li_{0.99}Ni_{0.83}Co_{0.12}Mn_{0.05}O_2$ ("NCM-prot(1%)"), with a BET surface area of 0.82 m^2 g_{NCM}^{-1}. Similarly, washing with a water-to-CAM ratio of 5 : 1 w/w leads to approx. 2 mol% protons in the NCM, equivalent to $H_{0.02}Li_{0.98}Ni_{0.83}Co_{0.12}Mn_{0.05}O_2$ ("NCM-prot(2%)", 1.08 m^2 g_{NCM}^{-1}). The structural analysis of these materials via XRD and subsequent Rietveld refinement revealed that the layered structure remains unchanged, with only a slight elongation of the c-lattice parameter (<0.5% change for a protonation of 25 mol%, cf. Fig. 5 and Table 4 in ref. 32). Furthermore, a batch of calcined NCM was prepared, which was heated at 525 °C in pure oxygen flow for 1 h ("NCM-calc", with a BET of 0.60 m^2 g_{NCM}^{-1}) and then transferred to an argon-filled glovebox (<0.1 ppm O_2 and H_2O, MBraun, Germany) without exposure to air. All material preparation, processing, and coating throughout the entire study was handled completely inertly in the argon-filled glovebox to avoid further reactions that could alter the amount of protons or form contaminants (e.g., Li_2CO_3) in/on the active materials.[25]

NCM working electrodes (WEs) were prepared by mixing the respective NCM materials, conductive carbon (carbon black Super C65, Timcal, Switzerland), and polyvinylidene fluoride (PVDF, Solef 5130, Solvay, Germany) as binder at a mass ratio of 96 : 2 : 2 with 37.5 wt% N-methyl-2-pyrrolidone (NMP, anhydrous, Sigma Aldrich, Germany). The slurry was mixed in a 20 mL ZrO_2 beaker using ten ZrO_2 beads (Ø 10 mm) in a ball mill (Pulverisette 7, Fritsch, Germany), using a sequential mixing procedure, where the slurry was mixed four times at 400 rpm for 5 min each, with 2 min rest intervals between each mixing step. The slurry was then coated onto the rough side of an aluminum foil (18 μm, MTI, USA) with a box-type coating bar (Erichsen, Germany) with a gap of 130 μm by hand in the argon-filled glovebox; the coatings were then dried in the glovebox at ambient temperature for ~24 h. For OEMS measurements, the slurry was coated by the same procedure onto a stainless-steel mesh (316 grade, 26 μm aperture, 25 μm wire diameter, The Mesh Company, UK). For the cathodes,

an areal loading of 10 ± 0.5 mg_{NCM} $cm^{-2}_{electr.}$ was achieved (the actual loadings were determined with a precision of ± 0.1 mg_{NCM} $cm^{-2}_{electr.}$).

For anodes, graphite counter electrodes (CEs) were prepared by mixing graphite T750 (SG3, SGL Company, Switzerland), sodium carboxymethylcellulose (Na-CMC; Sigma Aldrich, USA), and styrene–butadiene rubber (SBR; Zeon, Japan) as binder at a mass ratio of $97.0 : 1.5 : 1.5$ with 45 wt% deionized water (18 $M\Omega$ cm^{-1}, Milli-Q, Merck, Germany) using a planetary centrifugal mixer (ARV-310, Thinky Corp., USA), mixing two times for 10 min at 2000 rpm; as final step, the SBR was added, after which the slurry was mixed again for 2 min at 500 rpm. The slurry was coated onto the rough side of a copper foil (12 µm, MTI, USA) by using the box-type coating bar with a gap of 180 and 200 µm using an automated coater (RK PrintCoat Instruments, United Kingdom), and dried in air at ambient temperature for 12 h. For the graphite CEs, an areal loading of 7 ± 1 mg_{gra} $cm^{-2}_{electr.}$ was achieved.

For half-cell and full-cell tests, cathode ($\varnothing$ 10, 10.95, and 14 mm) and anode ($\varnothing$ 10.95 and 15 mm) electrodes were punched out (Hohsen, Japan) from the prepared electrode sheets. For the OEMS cell, LFP electrodes ($\varnothing$ 15 mm) were punched out from commercially available sheets (3.5 mAh $cm^{-2}_{electr.}$, Custom Cells, Germany). All cathode electrodes with an aluminum current collector were compressed at 200 MPa for 30 s using a KBr press (Mauthe Maschinenbau, Germany). All electrodes were then dried (separately for anodes, pristine cathodes, and washed cathodes) at 120 °C *in vacuo* (Büchi, Switzerland) for 6 h and transferred to the argon-filled glove box without exposure to air. As described in detail in the previous publication, protons are thermally released only if the temperature is increased above 140 °C (*cf.* Fig. 3 in ref. 32). In addition to that, intermixing of the protons from the near-surface layers with lithium ions from the bulk was excluded using XPS (Fig. S1 in the SI).

On-line electrochemical mass spectrometry (OEMS)

To avoid a contribution to the gas evolution from the CE,[6] delithiated $LiFePO_4$ (LFP) was used as CE for the OEMS experiments. Prior to cell assembly, the LFP electrode was delithiated to 90% SOC in a CR2032-type coin cell (Hohsen, Japan) with a lithium-metal CE (450 µm thickness, $\varnothing$ 15 mm, Rockwood, USA), two glass-fiber separators ($\varnothing$ 16 mm, glass-microfiber filter, 691, VWR, Germany) and one PP/PE/PP separator ($\varnothing$ 17 mm, H2013, Celgard, USA) that faced the LFP electrode. The coin cell was then filled with 120 µL LP57 (1 M $LiPF_6$ in EC : EMC 3 : 7 w/w, 1.7 ppm H_2O; BASF, Germany). The half-cell was cycled once between 3.0 and 4.0 V *vs.* Li^+/Li (= V_{Li}), before the LFP was charged to 90% delithiation ($Li_{0.1}FePO_4$) with a stable potential of 3.5 V_{Li}. The electrode was then harvested from the coin cell and transferred into the OEMS cell without further washing.

The OEMS cell was assembled according to Tsiouvaras *et al.*,[40] by placing the delithiated LFP at the bottom of the cell, followed by two PP/PE/PP separators ($\varnothing$ 24 mm), 100 µL LP57, and the respective uncompressed NCM cathode

($\varnothing$ 14 mm) as working electrode (WE). The OEMS cell was then placed into a climate chamber at 25 °C (T-40/25, CTS, Germany) and connected to an SP-300 potentiostat (BioLogic, France) and a mass spectrometer system (HiQuad QMH 400–1, Pfeiffer Vacuum, Germany). Before cell cycling, the cell was equilibrated for 4 h at open-circuit voltage (OCV), before it underwent a constant-voltage (CV) hold at 3.0 V_{Li} (corresponding to -0.6 V *vs.* LFP (= V_{LFP})), for 1 h. The cell potential was increased with a potential scan rate of 50 mV h^{-1} to an upper potential cutoff of 5.0 V_{Li} (≈ 1.5 V_{LFP}). Afterwards, the cells were calibrated using O_2 and CO_2 (each 2000 ppm) in argon (Westfalen AG, Germany). During data evaluation, all ion currents were normalized to the ^{36}Ar signal at $m/z = 36$, and gas concentrations were calculated *via* the calibration gas.

Half-cell testing with lithium-metal reference electrode

For the electrochemical testing in half-cells, spring-compressed T-cells (Swagelok, USA) were assembled using a lithium-metal CE ($\varnothing$ 11 mm), and a lithium-metal reference electrode (RE, $\varnothing$ 6 mm), three glass-fiber separators ($\varnothing$ 11 mm, two separators between CE and WE, one separator facing the RE), 90 µL LP57 electrolyte, and the respective compressed cathode WE ($\varnothing$ 10.95 mm). The cell was placed in a climate chamber (Binder, Germany) at 25 °C and connected to a battery cycler (Series 4000, Maccor, USA), while the potential was controlled between RE and WE.

To acquire the first-charge potential curve, the cell was cycled with a *C*-rate of *C*/50 to 5.0 V_{Li}. Note that, for all charge/discharge cycling, the *C*-rate is referenced to the theoretical capacity of the NCM831205 CAM of 275 mAh g_{NCM}^{-1}.

For the galvanostatic–intermittent–titration technique (GITT), the cells were charged/discharged with a constant current of *C*/15, whereby after each 0.5 h constant-current charge/discharge a 5 h open-circuit potential (OCP) rest phase was applied; to increase the resolution after the first relatively sharp increase in the potential curve, the first charge-OCP phase sequence was split into charging for 6 min, followed by the OCP period, and 24 min, again followed by the OCP period, accumulating to a total charge of 0.5 h. The WE potential was controlled *via* the RE and was set to 3.0 and 4.1 V_{Li}.

For the rate tests, the cells were cycled in the potential window of 3.0–4.1 V_{Li}, and each constant-current (CC) charge period was followed by a constant-voltage phase (= CCCV) with a current cutoff of *C*/20. The discharge cycling rate was then incrementally increased every three cycles from *C*/20 to *C*/10, *C*/5, *C*/2, 1*C*, 2*C*, 5*C*, 10*C*, and 20*C*. During charge, the rate was set the same as during discharge until *C*/2, while at higher discharge rates, the charge rate was kept at *C*/2. This rate test was then followed by 20 cycles with a charge rate of *C*/2 and a discharge rate of 1*C*, and three check-up cycles at *C*/10 for both charge and discharge.

Full-cell testing in coin-cells

For testing in full-cells, coin cells were assembled using an uncompressed graphite anode ($\varnothing$ 15 mm), one PP/PE/PP separator ($\varnothing$ 17 mm), 30 µL LP57 electrolyte, and the respective

compressed NCM WE (∅ 14 mm). For the first set of experiments, the cells were cycled in CCCV mode during charge, in CC mode during discharge in the potential range of 3.0–4.1 V $vs.$ graphite (V_{gra}), in the second set in the range of 3.0–4.6 V_{gra}. The graphite electrodes were not only chosen to be geometrically but also capacitively oversized (anode/cathode areal capacity ratio ("N : P") of 1.1 : 1); for the anode, a specific capacity of 355 mAh g_{gra}^{-1} was assumed, while, depending on the upper cutoff potential, a reversible cathode capacity of 180 and 250 mAh g_{NCM}^{-1} was used for 4.1 and 4.6 V_{gra}, respectively. Thus, anodes were chosen to match the required capacity for capacitive oversizing. The electrochemical procedure consisted of check-up cycles and aging: first, for the check-up cycles, all cells were cycled with two cycles at $C/15$ (charge and discharge), followed by a $C/15$ half-cycle to 3.8 V_{gra}, where 1 and 10 s $C/2$ DCIR discharge pulses were recorded, before the cell was discharged to 3.0 V_{gra}; then, for two cycles, the cells were charged at $C/2$, and discharged at $3C$. For the aging, the cells performed 36 cycles at $C/2$ (charge and discharge). This set of check-ups and aging was then repeated five times, before the procedure was completed by the set of check-up cycles at the end. Finally, a 1 h CV hold at 3.0 V_{gra} was added.

Full-cell testing with a micro-reference electrode

For electrochemical impedance spectroscopy (EIS), spring-compressed T-cells were built, where anode (∅ 10.95 mm) and cathode (∅ 10 mm) were chosen in accordance with the above-described specifications for full-cell tests, but instead of one PP/PE/PP separator, two glass-fiber separators (∅ 11 mm) were used, between which a gold-wire micro-reference (μ-RE, GWRE; Goodfellow Cambridge Ltd, United Kingdom) was inserted, as described by Solchenbach $et~al.$[41] The cell was then filled with 60 μL LP57 electrolyte. Prior to the experiment, the tip of the GWRE was lithiated, using a VMP3 multi-channel potentiostat (BioLogic, France), by applying 150 nA for 1 h between WE and RE, to reach a stable potential of the GWRE at 0.31 V_{Li}. The cells were then cycled in accordance with the above-described procedure for coin full-cells in a battery cycler, while, for the case of the T-cells, after each 10 s DCIR pulse, the cells were transferred into another climate chamber (25 °C, Binder, Germany) and connected to a multi-channel VMP3 potentiostat (BioLogic, France), where potentio-mode EIS (PEIS) measurements were conducted in the frequency range from 100 kHz to 100 mHz, with an amplitude of 15 mV, and 8 points per decade. The use of the GWRE allowed for a deconvolution of the full-cell spectrum (= WE−CE) into cathode (WE) and anode (CE) contribution. Subsequent to the PEIS, the above-described full-cell test was resumed. Impedance spectra were analyzed using the EC-Lab software (BioLogic, France, Version 11.52).

Elemental analysis

The aged graphite anodes were harvested from the cycled coin full-cells, and the electrode was removed from the current collector using a scalpel without previous washing. The analysis was performed by an external lab (Mikroanalytisches Labor Pascher, Germany) and carried out as described in a previous study.[42] In brief, the electrode powder was burned in an oxygen flow at 1200 °C while the resulting CO_2 was absorbed in sodium hydroxide solution to determine the carbon content by the conductivity change of the solution. For the quantification of lithium, nickel, cobalt, and manganese, the electrode powder was dissolved at 180 °C in a mixture of nitric acid and hydrochloric acid, from which the content of the four metals was determined via inductively coupled plasma atomic emission spectrometry (ICP-AES).

X-ray photoelectron spectroscopy (XPS)

For the post-mortem experiments, the cathodes were harvested from the cycled coin full-cells at the end of test, rinsed with EC : EMC (3 : 7 w/w, Gotion, USA), and stored in ~5 ml dimethyl carbonate (DMC, Sigma Aldrich, USA) for 24 h, before rinsing with fresh DMC again. For XPS measurements, electrodes were mounted conductively onto a stainless-steel stub, transferred into the device (Axis Supra, Kratos, UK) without exposure to ambient air, and pumped down to a pressure below 10^{-9} torr. The sample was irradiated using a monochromatic Al-K$_\alpha$ radiation with an energy of 1486.6 eV, using 15 mA emission current; the analyzer pass energy was set to 20 eV. The oxygen O 1s core level was investigated for the binding energies (BEs) between 537 and 527 eV using 10 sweeps with a step size of 0.1 eV and a dwell time of 200 ms, with active charge neutralization (0.45 A of filament current, 1 V of filament bias, 5 V of charge balance). Additionally, for verification, a survey spectrum (for BEs between 1202.5 and −7.5 eV at a pass energy of 160 eV, with a step size of 0.5 eV and a dwell time of 100 ms, using two sweeps), as well as the regions containing the C 1s, Ni 3p, Co 2p, and Ni 2p core levels (with a step size of 0.1 eV and a dwell time of 200 ms) were recorded (data not shown). For data analysis, the CasaXPS software (version 2.3.24, Casa Software Ltd) was used. After a Shirley background was subtracted, the core level spectra were deconvoluted by a Gaussian–Lorentzian fit function in a ratio of 70/30. The spectra were energy corrected to the adventitious-carbon peak at a binding energy of 284.8 eV.

Scanning electron microscopy (SEM)

For the top-view images of the electrodes, the electrodes were mounted onto a stainless-steel inert transfer holder (JEOL, Japan) using conductive copper tape (PPI Adhesive Products, Ireland) and transferred into the SEM (JSM-IT800, JEOL, Japan) without exposure to air. The images were recorded using a secondary-electron detector at an acceleration voltage of 5 kV.

Results & discussion

To investigate the impact of intercalated protons on the electrochemistry of a Ni-rich NCM (LiNi$_{0.83}$Co$_{0.12}$Mn$_{0.05}$O$_2$, further referred to as NCM831205), the pristine NCM ("NCM-prist") and the calcined NCM ("NCM-calc") will be

compared to two protonated NCMs, for which 1 or 2 mol% of Li^+ are ion-exchanged by H^+, resulting in $H_{0.01}Li_{0.99}MO_2$ ("NCM-prot(1%)") and $H_{0.02}Li_{0.98}MO_2$ ("NCM-prot(2%)"), respectively. Based on insights from our previous study on the protonation of the same NCM831205 material,[32] the protons intercalate and stay in the near-surface regions, forming a core–shell particle with a protonated surface layer (HMO_2) and a fully lithiated bulk ($LiMO_2$). Furthermore, electrode and cell preparation are not expected to affect the structure and composition of the NCMs since the protonated NCM is thermally stable up to 140 °C (*i.e.*, beyond the electrode drying temperature of 120 °C), thus maintaining the layered structure.[32]

On-line electrochemical mass spectrometry (OEMS)

To analyze if (and at which potential) protons deintercalate from the NCM electrochemically, OEMS is performed first. Here, the NCMs are charged in a custom-made cell while the gas evolution is tracked *via* an attached mass spectrometer.[40] To minimize the influence of kinetics, a potential sweep to 5.0 V_{Li} with a slow scan rate of 50 mV h^{-1} was applied (corresponding to a *C*-rate of approx. *C*/40 if the current was constant during the potential scan). Next to NCM as working electrode (WE), partially delithiated LFP ($LiFePO_4$, electrochemically delithiated to $Li_{0.1}FePO_4$) was used as counter electrode (CE), providing a stable potential and no/little gas evolution, as already described in previous studies.[43,44] For easier comparability, all potentials are given with respect to the Li^+/Li reduction potential (denoted as V_{Li}) by considering the potential of the $Li_{0.1}FePO_4$ CE of 3.5 V_{Li}.

The results obtained by OEMS are shown in Fig. 1, where, in Fig. 1a, the specific current, normalized to the respective mass of the NCM831205 material, is plotted both as a function of time (lower *x*-axis) and of the NCM potential *vs.* Li^+/Li (V_{Li}, upper *x*-axis). When the potential scan is applied, the first redox peak appears at 3.62 V_{Li} for NCM-calc and at 3.65 V_{Li} for NCM-prist, where the phase transition from hexagonal (H1) to monoclinic (M) occurs.[5,45] The observed peak splitting hints at the presence of two phases.[45] Both protonated NCMs undergo the same phase transition but at higher potentials: that of NCM-prot(1%) is shifted positively to 3.70 V_{Li}, and that of NCM-prot(2%) is shifted to 3.77 V_{Li}. Likely due to this apparent overpotential, the peak splitting observed for NCM-calc and NCM-prist is no longer visible. When the potential is increased further, the current profiles of the four materials align again, exhibiting the same redox peak at ~4.0 V_{Li} for the transition from the M phase to the second hexagonal phase (H2).[5,45] Similarly, at ~4.3 V_{Li}, all four materials undergo the phase transition from H2 to the third hexagonal phase (H3),[5,45] whereby an increasing proton content leads to a small additional positive shift in potential. The redox feature present at 4.6 V_{Li} for NCM-prist and NCM-calc is missing for the protonated samples, which consequently reduces their capacity at high potentials. Initially, we believed the feature could stem from a parasitic reaction of a surface contaminant that gets oxidized in case of the unwashed NCMs. This could not be proven through a separate experiment, where, for a very briefly
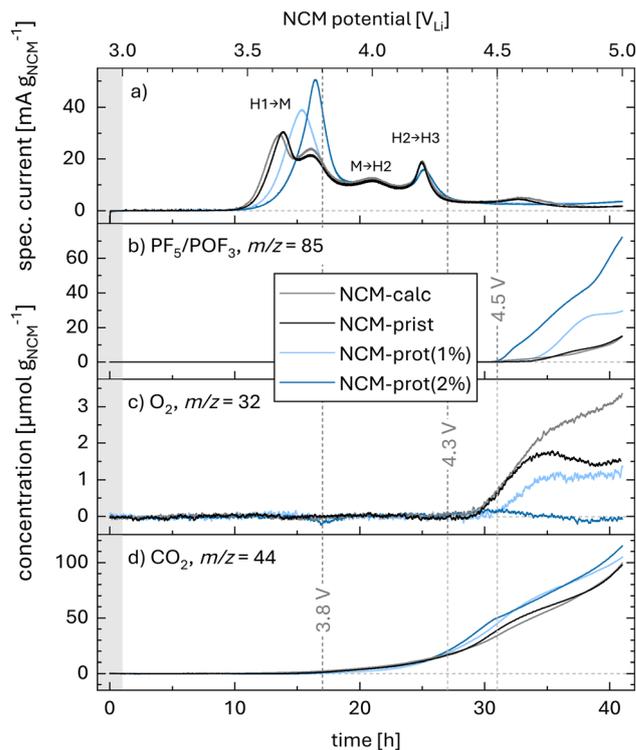

Fig. 1 First-charge current and concomitant gas evolution determined by OEMS measurements at 25 °C as a function of NCM831205 WE potential (upper *x*-axis) and time (lower *x*-axis), using an OEMS cell assembled with NCM-calc (gray), NCM-prist (black), NCM-prot(1%) (light blue), or NCM-prot(2%) (dark blue) as WE, and cycled *vs.* a partially delithiated, capacitively oversized LFP CE (with two Celgard H2013 separators and 100 μL LP57 electrolyte). The cell potential was held constant at 3 V_{Li} for 1 h (gray area) and then scanned using a linear potential sweep at 50 mV h^{-1} to 5.0 V_{Li}, (= 1.5 V_{LFP}), while the gas evolution was recorded by mass spectrometry. (a) Specific current (*i.e.*, current normalized by the NCM mass). Total concentrations of evolved gases normalized by the total NCM mass in the OEMS cell: (b) PF_5 and/or POF_3 recorded on mass channel *m/z* = 85; (c) molecular oxygen (O_2, *m/z* = 32); and, (d) carbon dioxide (CO_2, *m/z* = 44). The vertical dashed gray lines indicate the onset potential of the CO_2 evolution (3.8 V_{Li}), the O_2 evolution (4.3 V_{Li}), and the PF_5/POF_3 evolution (4.5 V_{Li}).

washed sample (*i.e.*, low proton content, low amount of residual surface contaminants), that redox peak is still present (data not shown). Though the reason behind this absence remains unclear, we conclude that it is an effect of the presence of protons in the NCM structure rather than the absence of contaminants from its surface. A detailed discussion of the effect of the protons on the NCM potential curve and its origins is provided for the discussion of Fig. 3.

Next, the gases evolving during the first charge are discussed. First, in Fig. 1b, the mass trace *m/z* = 85 is depicted, which was shown to correspond to the POF_2-moiety of either PF_5 and/or POF_3 gas (labelled in the following as PF_5/POF_3), as explained by Solchenbach *et al.*[46] These species derive from the different decomposition pathways of the $LiPF_6$ salt, which will be detailed in the following. For the hydrolysis of the $LiPF_6$ salt in a LIB electrolyte,[47,48] trace amounts of PF_5, being

in equilibrium with dissolved but non-dissociated $LiPF_6$ (eqn (2)), react with H_2O, that has been shown to originate from the chemical oxidation of the electrolyte (eqn (3)):[27,49,50]

$$LiPF_6 \leftrightarrow PF_5 + LiF \qquad (2)$$

$$PF_5 + H_2O \rightarrow POF_3 + 2HF \qquad (3)$$
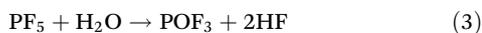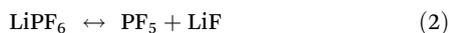
In a first step, this leads to the formation of POF_3 and HF. However, Stich et al.[47] showed via acid–base titration and ion-chromatography that the produced POF_3 undergoes a fast hydrolysis to non-volatile HPO_2F_2 and further HF, so that POF_3 is a relatively short-lived intermediate in the overall hydrolysis reaction (eqn (4)):

$$POF_3 + H_2O \rightarrow HPO_2F_2 + HF \qquad (4)$$
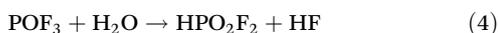
The initial formation of POF_3 via eqn (3) and its subsequent gradual consumption via eqn (4) was recently validated by OEMS experiments for a LIB electrolyte (1 M $LiPF_6$ in EC/DEC) spiked with different amounts of H_2O.[51]

In contrast to its relatively slow hydrolysis, the PF_6^- ion can also undergo a fast reaction with protic species in the electrolyte, as demonstrated by the rapid decomposition of $LiPF_6$ in an LIB electrolyte upon addition of methanesulfonic acid (eqn (5)):[46]

$$PF_6^- + H^+ \rightarrow PF_5 + HF \qquad (5)$$
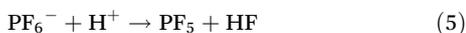
Due to the fast reaction kinetics of protons with PF_6^-, a release of protons from the NCM is expected to be accompanied by the rapid formation of PF_5. As the formed PF_5 will react with H_2O impurities in the instrumentation, it will be detected readily as POF_3 on mass channel $m/z = 85$ by OEMS.[46] Please note that the hydrolysis of POF_3 to HPO_2F_2 is expected to only occur with a surplus of H_2O, and not within the instrumentation, and therefore we assume that all signal on mass channel $m/z = 85$ is can be linked exclusively to the proton release.[46,51] By this approach, it was also shown that the electrochemical oxidation of $LiPF_6$ in LIB electrolytes at high cathode potentials leads to the formation of protons.[46,49,52] Consequently, while any signal on mass channel $m/z = 85$ that is obtained for the proton-free NCM-calc material likely originates from the electrochemical electrolyte oxidation and may serve as a background, an additional signal from the protonated NCMs is likely linked to the release of protons into the electrolyte.

To summarize, the deintercalation of protons from the NCM structure in the form of H_2O/H^+ will lead to a depletion of the conductive salt in the electrolyte; if $LiPF_6$ is decomposed by H_2O, no signal on the mass channel $m/z = 85$ is to be expected as the formed POF_3 is hydrolyzed into HPO_2F_2 quickly (eqn (2)–(4)). On the other hand, if $LiPF_6$ is decomposed via H^+, PF_5 is formed, that can be detected on the mass channel $m/z = 85$ (eqn (5)), while NCM-calc serves as background for the evaluation of the PF_5 signal contribution that is ascribed to the release of intercalated protons from the protonated NCMs (NCM-prot(1%) and NCM-prot(2%)).

As depicted in Fig. 1b, no signals are observed at $m/z = 85$ up to a cathode potential of ~4.7 V_{Li} for both NCM-prist and NCM-calc; at higher potentials, the signals at $m/z = 85$ increase, reaching an amount equating to 6.2 $\mu mol_{PF_5} \ g_{NCM}^{-1}$ by the end of test (EOT) at 5 V_{Li}. On the other hand, the protonated materials NCM-prot(1%) and NCM-prot(2%) show an earlier onset potential for PF_5/POF_3 evolution at ~4.5 V_{Li}; by EOT at 5.0 V_{Li}, both materials yield a higher total amount of PF_5, namely 30 $\mu mol_{PF_5} \ g_{NCM}^{-1}$ (NCM-prot(1%)) and 72 $\mu mol_{PF_5} \ g_{NCM}^{-1}$ (NCM-prot(2%)). The additional amount of PF_5 of the protonated NCMs must stem from the deintercalation of H^+ from the protonated NCMs and their fast reaction with PF_6^- (see eqn (5)). This proton-induced, accelerated depletion of the conductive salt is expected to negatively impact the electrochemical performance,[17] which will be revisited within the context of the full-cell data. Thus, we ascribe the onset of PF_5 evolution at 4.5 V_{Li} for the NCM-prot(2%) material to the onset for the electrochemical deintercalation of protons, analogous to the electrochemical deintercalation of lithium ions (eqn (6)):

$$H_xMO_2 \rightarrow MO_2 + x \cdot H^+ + x \cdot e^- \qquad (6)$$

It has to be noted that the observed onset potential may depend on the degree of delithiation, on the composition and the nickel content of the CAM, as well as on the initial proton content after washing. The observed release of protons corresponds to an SOC of ~88%; a separate experiment with a faster scan rate of 150 mV h^{-1} revealed the same SOC for the onset of PF_5 detection, despite a slightly higher potential of 4.7 V_{Li} (data not shown). Hence, the release of the protons seems to be tied to the degree of delithiation, yet a more thorough study is beyond the scope of this work. Nonetheless, this onset potential agrees well with the electrochemical potential of the deprotonation of $Ni(OH)_2$ to NiOOH, which occurs in an aqueous electrolyte at approx. 1.3 V_{SHE}, corresponding to ~4.4 V_{Li}.[53]

Next, the amount of molecular oxygen (O_2, $m/z = 32$), depicted in Fig. 1c, is analyzed: the release of O_2 from NCM831205 occurs at 4.4 V_{Li} for NCM-calc, which corresponds to a capacity of 220 mAh g_{NCM}^{-1}, respectively ~80% SOC (based on a theoretical capacity of 275 mAh g_{NCM}^{-1}), in agreement with previous studies of Ni-rich active materials.[5,6] In total, NCM-calc evolves 3.5 $\mu mol_{O_2} \ g_{NCM}^{-1}$ at EOT. NCM-prot(1%) has a slightly delayed onset for O_2 evolution and only yields 1.4 $\mu mol_{O_2} \ g_{NCM}^{-1}$, which is about 60% less than that of NCM-calc. For the more strongly protonated NCM-prot(2%), no significant amount of evolved O_2 is observed at all at EOT.

One could speculate that the substantially reduced/completely absent evolution of O_2 of the protonated NCMs could stem from an oxygen depletion of the NCM prior to cell cycling, i.e., during washing and drying. However, it was already shown by Pritzl et al.[31] that no molecular oxygen is released from a nickel-rich NCM upon washing with water. Similarly, we also observed the retention of a fully layered structure in our previous study when drying the washed CAMs at temperatures

below 140 °C, even for high degrees of protonation.[32] The amount of detected oxygen is also tied closely to the morphology, where the exposure of initially closed pores to the electrolyte after washing facilitates the reaction of the released oxygen with the electrolyte, as reported before for the comparison of poly- and single-crystalline NCM622.[44] Since the slurry was prepared using a ball-milling process, agglomerates are mostly separated and pores are expected to be equally accessible for the washed and unwashed NCMs (see BET values of CAM powder and electrodes as well as SEM images in the SI, Fig. S2). Based on these observations, the loss of oxygen from the near-surface region of the NCM particles upon washing and drying is considered to be negligible.

It seems more likely that, due to the presence of protons in the NCM, the protons react with the oxygen from the NCM, resulting in the formation of water, an oxygen-depleted surface ($MO_{x<2}$), and the nominal reduction of the TMs, similar to the thermally induced decomposition of the protonated phase (eqn (7)):[32]

$$H_x MO_2 \xrightarrow{U > 4.5\,V_{Li}} \left(1 - \frac{x}{2}\right) MO_2 + \frac{x}{2} MO + \frac{x}{2} H_2O \quad (7)$$
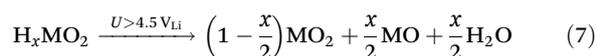
In the case of NCM-prot(1%), for which ∼70% less O_2 is evolved compared to NCM-prist, the near-surface lattice oxygen, which typically evolves at high SOC, reacts with intercalated protons to water instead. While the released H_2O would hydrolyze $LiPF_6$, it would likely not be detected by OEMS due to the low concentration of the intermediate POF_3 (see above discussion of eqn (2)–(4)). Based on this hypothesis, the small amount of O_2 detected for NCM-prot(1%) would be lattice oxygen evolving from pristine, formerly lithiated MO_2 layers underneath the protonated HMO_2 phase; in other words, the amounts of protons intercalated in NCM-prot(1%) appears to not be sufficient for the complete conversion of the oxygen that is released upon the surface reconstruction of the CAM at high SOC into H_2O. This would be consistent with the observation that no molecular oxygen is observed at all for the more protonated NCM-prot(2%): in this case, the thicker layer of HMO_2 at the surface of the CAM particles,[32] appears to allow for a complete transformation of the oxygen, which is released upon the formation of a rock-salt-type surface phase, to H_2O. For these hypotheses to be plausible, the amounts of protons in NCM-prot(1%) would have to be enough to convert the missing amount of evolved O_2 when compared to NCM-calc, namely the difference of 2.1 $\mu mol_{O_2}\,g_{NCM}^{-1}$. This is indeed the case, as 1 mol% of protons in NCM-prot(1%) correspond to 85 $\mu mol_{H^+}\,g_{NCM}^{-1}$, which could potentially consume 42.5 $\mu mol_{O_2}\,g_{NCM}^{-1}$, i.e., substantially more than the missing 2.1 $\mu mol_{O_2}\,g_{NCM}^{-1}$. In turn, this would imply that only a small fraction of the intercalated protons is released as water, while the majority would have to be released as protons into the electrolyte or remain within the CAM lattice. This is supported by the observation that ∼15 $\mu mol_{PF_5}\,g_{NCM}^{-1}$ more PF_5 is detected at a potential of 4.8 V_{Li} for the NCM-prot(1%) compared to NCM-calc (see Fig. 1b). In summary, to the best of our knowledge, the formation of an oxygen-depleted surface

layer upon the electrochemically induced proton release has not yet been discussed in the literature and points towards a novel degradation mechanism for protonated NCMs. This hypothesis will be revisited later in this publication, where the surface of cycled electrodes is analyzed by XPS (see Fig. 7).

Finally, the evolution of carbon dioxide (CO_2, $m/z = 44$), depicted in Fig. 1d, shows that the onset for CO_2 evolution appears at 3.8 V_{Li} for all materials, which is likely due to the oxidation of electrolyte impurities to protons and their subsequent reaction with Li_2CO_3 surface impurities to CO_2.[27,54] The total CO_2 amount at EOT at 5.0 V_{Li}, which includes the CO_2 originating from the chemical oxidation of the electrolyte solvents with oxygen released from the NCM lattice,[5,13,14] is similar for all NCMs (100, 119, 105, and 115 $\mu mol_{CO_2}\,g_{NCM}^{-1}$ for NCM-calc, NCM-prist, NCM-prot(1%), and NCM-prot(2%), respectively). Interestingly, the protonated materials evolve slightly more CO_2 than the unwashed, non-protonated materials, while less oxygen is detected. This could be linked to the change in morphology upon washing, with the washed materials exhibiting a ∼10–30% higher specific surface area due to a partial separation of the primary CAM particles (see SEM images, Fig. S2).[44] Nonetheless, as the difference between the detected concentrations is close to the expected error from the measurement, a definitive explanation is omitted here.

To conclude the findings from the OEMS analysis, the protons present in the NCM deintercalate at cathode potentials beyond 4.5 V_{Li}, and at least a part of the protons likely leave the lattice in the form of H_2O. The potential of the H1 → M phase transition shifts positively for the first charge of the protonated NCMs, which also show less capacity at potentials beyond 4.5 V_{Li}. To elucidate the origin of the potential shift –whether it is a kinetically limited process, resulting in an overpotential, or a change in the (thermodynamic) open-circuit-potential (OCP) curve– the potential profile of the first charge is analyzed next.

First-charge potential curve

To assess the effect of the protonation of the NCM831205 CAMs on their available capacity, the first-charge curve is shown in Fig. 2. To minimize the influence of kinetics, the NCMs are charged with a slow rate of $C/50$, and the potential is controlled vs. the lithium-metal reference electrode (RE). The initial cathode OCP is very similar for all cells (3.1–3.2 V_{Li}), and no trends between the non-protonated and protonated NCMs can be observed. Exemplarily, the OCP of NCM-prot(2%), which corresponds to a degree of lithiation of 98% and a formal SOC of 2% ($H_{0.02}Li_{0.98}MO_2$), is 3.2 V_{Li}. If this is compared to the recorded potential curve of NCM-calc, the potential at 2% SOC ($Li_{0.98}MO_2$) equals 3.6 V_{Li}, which is much higher than the OCP of NCM-prot(2%). This indicates that a 2% replacement of the intercalated Li^+ by H^+ does not have the same effect on the NCM potential as a mere 2% electrochemical delithiation, i.e., that the initial OCP of the NCM does not depend on its proton content. This means that the electrochemical potential of Li^+ in the protonated NCM is
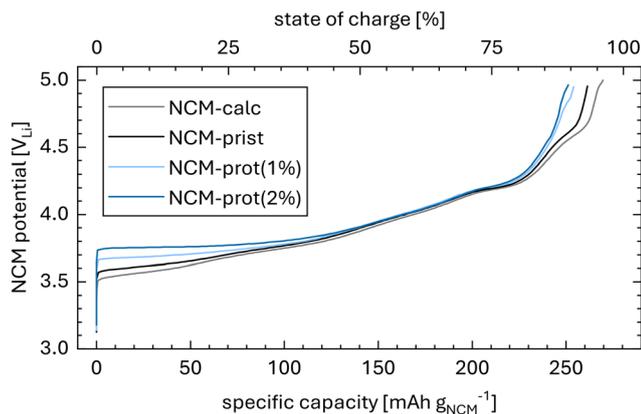
Fig. 2 First-charge potential profiles of the NCM831205 CAMs as a function of both the specific capacity (lower *x*-axis) and the state of charge (upper *x*-axis), with NCM-calc (gray), NCM-prist (black), NCM-prot(1%) (light blue), and NCM-prot(2%) (dark blue) as WE. The T-cells were charged with a constant current of $C/50$ (based on a theoretical capacity of 275 mAh g_{NCM}^{-1}) *vs.* metallic lithium in a half-cell configuration at 25 °C, whereby the potential was controlled *vs.* the Li-RE to an upper cathode potential cutoff of 5.0 V_{Li}. The cells were built using two glass-fiber separators between CE and WE, and one facing the RE, adding 30 μL LP57 electrolyte to each separator.

apparently unaffected by the protons in the protonated shell and that the cation exchange does not induce a change of oxidation state of the transition metals.

Upon delithiation, NCM-calc and NCM-prist exhibit a sloped potential profile and reach a total capacity of 269.6 and 262.2 mAh g_{NCM}^{-1} at 5.0 V_{Li}, which equals 98% and 95% of the theoretical capacity of 275.0 mAh g_{NCM}^{-1}, respectively. The potential profile exhibits all reported phase changes, as already discussed for the specific currents measured in the OEMS (Fig. 1a). On the other hand, during the charge of NCM-prot(1%), a plateau-like region at ~3.7 V_{Li} is noticeable in the low-SOC range, with a potential offset with respect to NCM-prist of ~100 mV. This difference is even more pronounced for NCM-prot(2%), where the potential offset is increased to 150–200 mV. This potential offset is consistent with the potential shift of the first redox peak (H1 → M phase transition) observed during the OEMS experiment (Fig. 1a). To quantify these differences, the mean, charge-averaged NCM potential during the first charge in the SOC window from 0–50% is calculated, which equates to 3.67, 3.68, 3.72, and 3.77 V_{Li} for NCM-calc, NCM-prist, NCM-prot(1%) and NCM-prot(2%), respectively. Thus, in this experiment, the first-charge overpotential in the low-SOC region increases by approx. 50 mV for each 1 mol% of inserted protons. A detailed discussion of the effect of the protons on the NCM potential curve and its origins is provided for the discussion of Fig. 3.

Starting at ~4.0 V_{Li} or ~150 mAh g_{NCM}^{-1}, the potential curves of all NCMs align with each other, until the NCM potential reaches ~4.2 V_{Li}, or ~210 mAh g_{NCM}^{-1}, where the potential curves start to deviate from each other again, particularly after ~4.5 V_{Li}, coinciding with the above discussed deintercalation of the protons. This potential offset persists until 5.0 V_{Li},

where a specific capacity of 255.1 mAh g_{NCM}^{-1} for NCM-prot(1%), and of 253.0 mAh g_{NCM}^{-1} for NCM-prot(2%) is obtained, which agrees with the respective capacities observed in the OEMS experiment (see Fig. 1a). The differences in capacity could stem from the removal of cyclable lithium during the Li$^+$/H$^+$ ion exchange, and simply less lithium can be extracted, leading to a smaller capacity. This is however unlikely since 1–2 mol% of removed lithium corresponds to 3–6 mAh g_{NCM}^{-1} based on the theoretical capacity, while the measured differences between NCM-calc and the protonated NCMs of ~15–17 mAh g_{NCM}^{-1} are significantly larger. To elucidate this effect, a more detailed study of the side reactions with the electrolyte would be necessary, which is beyond the scope of this work. Nonetheless, to explore the apparent potential offset in the low-SOC region of the protonated NCMs, galvanostatic-intermittent-titration technique (GITT) is performed next.

Galvanostatic-intermittent-titration technique (GITT)

For this, the NCM WEs were cycled with a rate of $C/15$ in constant-current (CC) mode, and a 5 h OCP rest phase was introduced every 0.5 h (*i.e.*, in steps of 5% SOC) to allow for the determination of the open-circuit potential as a function of SOC. Cycling was performed between 3.0–4.1 V_{Li}, where ion-exchanged protons are expected to remain in the active material (Fig. 1). Fig. 3a compares the determined potential profile *vs.* time for the NCM-calc (gray lines) and the NCM-prot(2%) materials (blue lines). For a more rigorous comparison of the equilibrium potentials at a given SOC, the OCP values at the end of each 5 h OCP period are extracted and plotted as a function of capacity in Fig. 3b (cycle 1) and Fig. 3c (cycle 2).

In the first charge up to 3.75 V_{Li}, the potential differences between the CC and OCP phases of the NCM-calc material, *i.e.*, the overpotentials, range between ~30–60 mV; beyond this initial charge to 3.75 V_{Li} as well as in the subsequent charge/discharge cycles, the overpotential decreases to below 30 mV. In contrast, the NCM-prot(2%) material exhibits a rather high potential plateau at ~3.75 V_{Li} during the first eight CC/OCP cycles, while the NCM potential drops by ~200–250 mV over each 5 h OCP phase, closely approaching the OCP values obtained for the NCM-calc material. Over the first eight CC/OCP periods, *i.e.*, over the first ~96 mAh g_{NCM}^{-1} of charge, the potential of the NCM-prot(2%) material decreases gradually, while the one of the NCM-calc material increases, following the typical voltage *vs.* capacity profile. At higher SOCs, the potential drop of the NCM-prot(2%) material during the OCP periods decreases to ~20–30 mV, so that both its OCP drop and the overall potential curve become nearly identical to that of the NCM-calc material. Owing to these observations, it is concluded that the offset of the first-charge profiles of the protonated NCMs in the low-SOC region (Fig. 2) represents an apparently increased overpotential, and that the true OCP curve of the NCM remains unchanged upon protonation. Thus, the first-charge capacity of NCM-calc (192.4 mAh g_{NCM}^{-1}) is 4 mAh g_{NCM}^{-1} higher than that of NCM-prot(2%) (188.5 mAh g_{NCM}^{-1}), while the shape of the OCP curves remains essentially identical. In the subsequent cycle, the
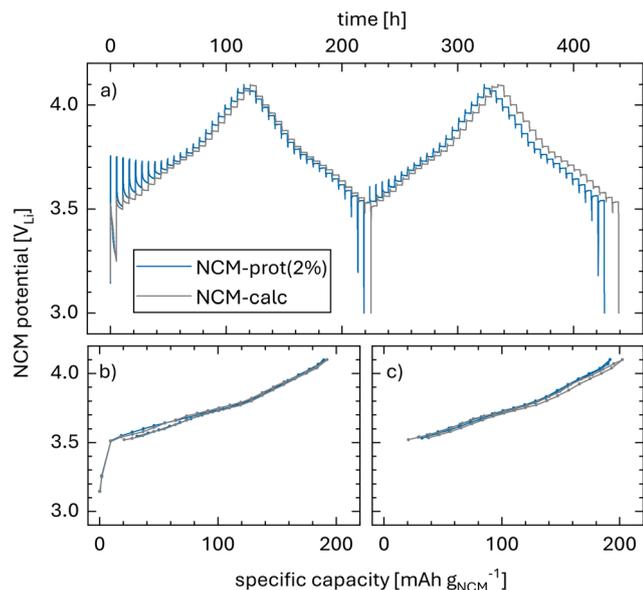
Fig. 3 GITT analysis for NCM-calc (gray) and NCM-prot(2%) (dark blue) as WEs in a T-cell half-cell setup with two glass-fiber separators between Li-CE and Li-WE, and one facing the RE, with 30 μL LP57 electrolyte on each separator. The cells were charged/discharged at 25 °C with a constant current of $C/15$ (based on a theoretical capacity of 275 mAh g_{NCM}^{-1}), whereby after each 0.5 h of constant-current period, a 5 h OCP rest phase was applied. In both charge/discharge cycles, the cathode potential cutoffs were set to 3.0 and 4.1 V_{Li}. (a) NCM potentials (measured *vs.* the RE) as a function of time. Equilibrated NCM potential at the end of each of the 5 h OCP periods *vs.* the specific capacity (in mAh g_{NCM}^{-1}) for (b) cycle 1 and (c) for cycle 2.

initially higher overpotential for the NCM-prot(2%) material has vanished, and the relaxation during the OCP phases seems relatively similar for both NCM-prot(2%) and NCM-calc.

To align all observations, the following hypothesis is proposed: As shown by XPS in our previous work, protons intercalate into the near-surface layers of the NCM upon washing.[32] This protonated HMO_2 shell around the NCM particles then causes a kinetic hindrance for lithium deintercalation in the form of a diffusion barrier, as also noted by Wan *et al.*,[55] resulting in the higher overpotential in the low-SOC region during the first charge. After a certain extent of delithiation, the empty lithium sites provide vacancies for both lithium ions and protons to become more mobile, and the protons start to distribute within the particle, potentially reaching a homogeneous distribution within the NCM particles at the end of charge. After having extracted about 150 mAh g_{NCM}^{-1}, the protons can redistribute within the NCM particle, removing the kinetic barrier for the lithium extraction, which is why the potential curves realign again (see Fig. 2) and the M → H2 phase transition at about 4.0 V_{Li} is unaffected by the remaining protons (see Fig. 1a). After having extracted about 210 mAh g_{NCM}^{-1}, the current of the H2 → H3 phase transition at about 4.2 V_{Li} is reduced (see Fig. 1a), and the potential curves start to deviate again beyond 4.2 V_{Li} (see Fig. 2). A shortened plateau of the H2 → H3 phase transition has been attrib-

uted to the presence of nickel ions in the lithium layer.[56] Even though the nickel disorder could be excluded for the protonated but uncharged NCM material in a previous study,[32] the intercalated protons may facilitate a migration of the nickel ions when lithium ions have been removed electrochemically, potentially resulting in the observed decrease of the available capacity during the H2 → H3 phase transition and beyond.

In the subsequent cycle, the absence of the overpotential in the low-SOC region does not mean that the protons have deintercalated, but that they do not longer cause a kinetic barrier for the solid-state lithium diffusion, as there is no diffusion-inhibiting protonated shell (*cf.* visual summary later in the publication in Scheme 1, middle panel). Since there is no proton deintercalation at potentials during the first charge below 4.5 V_{Li}, as suggested by the OEMS analysis in Fig. 1, the protons that remain in the NCM structure after the first cycle to 4.1 V_{Li} apparently do not affect the performance in the subsequent cycle. To examine whether the remaining protons affect the rate performance and the capacity retention, a discharge rate test is performed next.

Discharge rate test

To investigate the effect of the protonation of the NCMs on the rate capability, a discharge rate test was performed, using a three-electrode half-cell setup with lithium metal as CE, while the NCM potential was controlled *vs.* a lithium-metal RE. The applied potential window of 3.0–4.1 V_{Li} was kept well below the onset potential for both the deintercalation of the protons as well as the release of lattice oxygen (Fig. 1), and the discharge rate was increased incrementally every three cycles from $C/20$ to $20C$. The results of the discharge rate test are shown in Fig. 4a where the discharge capacities are plotted as a function of cycle number. At $C/20$, all materials deliver a similar capacity of 170.7, 168.5, 167.0, and 165.2 mAh g_{NCM}^{-1} for NCM-calc, NCM-prist, NCM-prot(1%) and NCM-prot(2%), respectively, while the discharge capacity seems to be slightly decreased with increasing proton content even at this low C-rate. The potential curve of the third cycle at $C/20$ is plotted in Fig. 4c: None of the materials exhibit a significant overpotential in the low-SOC region –unlike during the first charge (Fig. 2 and 3a)– and only NCM-prot(2%) shows a slightly decreased capacity. When increasing the discharge rate, more pronounced differences between the NCM materials can be observed, with the discharge capacities decreasing with increasing proton content. To illustrate this observation more clearly, the discharge capacity of the third cycle of each C-rate is extracted and plotted as a function of C-rate in Fig. 4b; since the performance at high C-rates is no longer only governed by the NCM cathode but contributions from, *e.g.*, the ionic transport properties of the electrolyte, come into play,[57] it is only plotted up to a C-rate of $2C$. Here, it becomes clear that a higher degree of protonation causes a higher relative discharge-capacity loss with increasing discharge rates, with a difference of 5.5 mAh g_{NCM}^{-1} between NCM-calc and NCM-prot(2%) at $C/20$, 10.0 mAh g_{NCM}^{-1} at $C/2$, and 13.9 mAh g_{NCM}^{-1} at $2C$. The potential curves of the third cycle
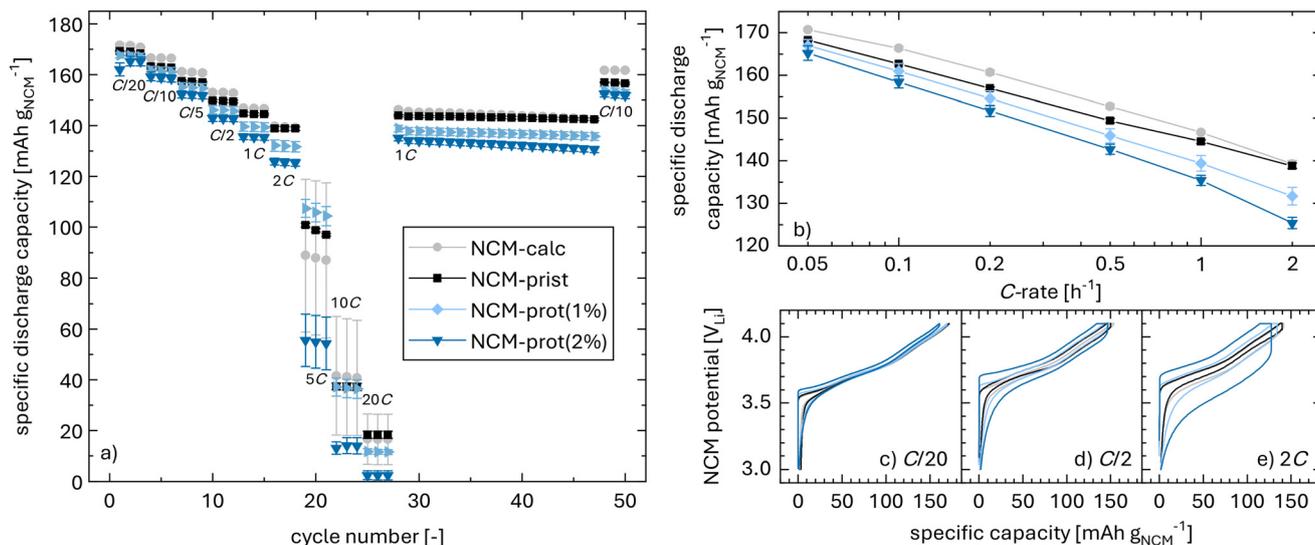
Fig. 4 Discharge rate test of NCM-calc (gray), NCM-prist (black), NCM-prot(1%) (light blue), and NCM-prot(2%) (dark blue) working electrodes in a T-cell half-cell setup at 25 °C, where the cathode potential range was set to 3.0–4.1 V_{Li} and controlled *vs.* the metallic lithium RE. The discharge rate was incrementally increased every three cycles from $C/20$ to 20C, while the charge rate was increased symmetrically until $C/2$, while it was kept constant at $C/2$ for higher discharge rates (note that C-rates are referenced to the theoretical NCM capacity of 275 mAh g_{NCM}^{-1}). The cells were assembled using two glass-fiber separators between CE and WE, and one facing the RE, with 30 μL LP57 electrolyte for each separator. (a) Specific discharge capacity *vs.* cycle number. (b) Specific discharge capacity for the third cycle at each C-rate, plotted *vs.* the C-rate on a logarithmic scale. (c–e) Selected NCM potential profiles *vs.* specific capacity, plotted for the third cycle at $C/20$, $C/2$, and 2C, (cycles 3, 12, and 18). All values are based on two nominally identical cells, and the error bars represent the minimum/maximum values.

at $C/2$ are shown in Fig. 4d, and the ones of the third cycle at 2C are shown in Fig. 4e. In both cases, it becomes apparent that a faster C-rate results in a significantly higher overpotential with increasing proton content, causing the potential curves during charge and discharge to evidently separate. Additionally, during the CV hold at the end of charge, more capacity is being provided for a higher degree of protonation, until the $C/20$ current-cutoff criterion is reached, hinting towards an increased resistance within the CAM. When the discharge rate is set to 1C after the rate test for aging, again, a smaller discharge capacity is measured with increasing proton content. This is also true for the appended $C/10$ check-up cycle at EOT: at beginning of test (BOT), the difference in capacity between NCM-calc and NCM-prot(2%) during the third $C/10$ cycle is 8.0 mAh g_{NCM}^{-1}, which increases to 10.0 mAh g_{NCM}^{-1} (−6.1%) at EOT.

To summarize, two main conclusions can be drawn from the rate-test experiments: (i) intercalated protons decrease the rate capability, as the presence of protons in the lithium layer might impair the solid-state diffusion of the intercalated lithium ions. This holds true even if the protons were distributed homogeneously throughout the NCM particle upon charge/discharge cycling, showing as an increased resistance. This proton-induced resistance increase seems plausible, as the decrease of rate capability seems to scale with proton content. (ii) Intercalated protons cause an accelerated capacity fading. For this degradation, several modes can be considered, namely impedance build-up, the loss of lithium inventory (LLI), or loss of active material (LAM). LLI can be excluded, as

the cathodes were tested in a half-cell configuration with an excess of lithium inventory. To evaluate the impact of LAM, an "inverse" rate test was performed, *i.e.*, that, instead of an increasing C-rate, the C-rate was decreased from high to low C-rates: after the initial three $C/20$ cycles, three cycles were conducted at a discharge rate of 20C, after which the discharge rate was incrementally decreased (see Fig. S3 in the SI). Here, the capacities at high rates are higher than in the normal rate test, and smaller at slower rates, which in the inverse rate test were cycled at the end of the rate test. In other words, cycles performed earlier in the experiment seem to perform better than later cycles, being indicative of either LAM and/or an increase in cathode impedance over the course of cycling. As observed by Hartmann *et al.*,[17] a possible proton-induced depletion of LiPF$_6$ could also cause a decline in rate capability; though as the protons should still be intercalated in the material, the reaction mechanism is unclear. To shed light on the effect of the protonation on the proposed degradation mechanisms, the protonated NCMs will be evaluated next upon extended cycling in a practically relevant full-cell configuration with a graphite anode.

Full-cell cycling

For the full-cell experiments, the four different NCM cathodes were cycled *vs.* a graphite anode in a coin-cell setup without reference electrode. Two sets of experiments were performed: in the first set, the cutoff voltages of 3.0 and 4.1 V_{gra} (note that the upper cutoff voltage corresponds to an NCM potential of 4.15 V_{Li}, assuming a graphite electrode potential of 0.05 V_{Li}, in
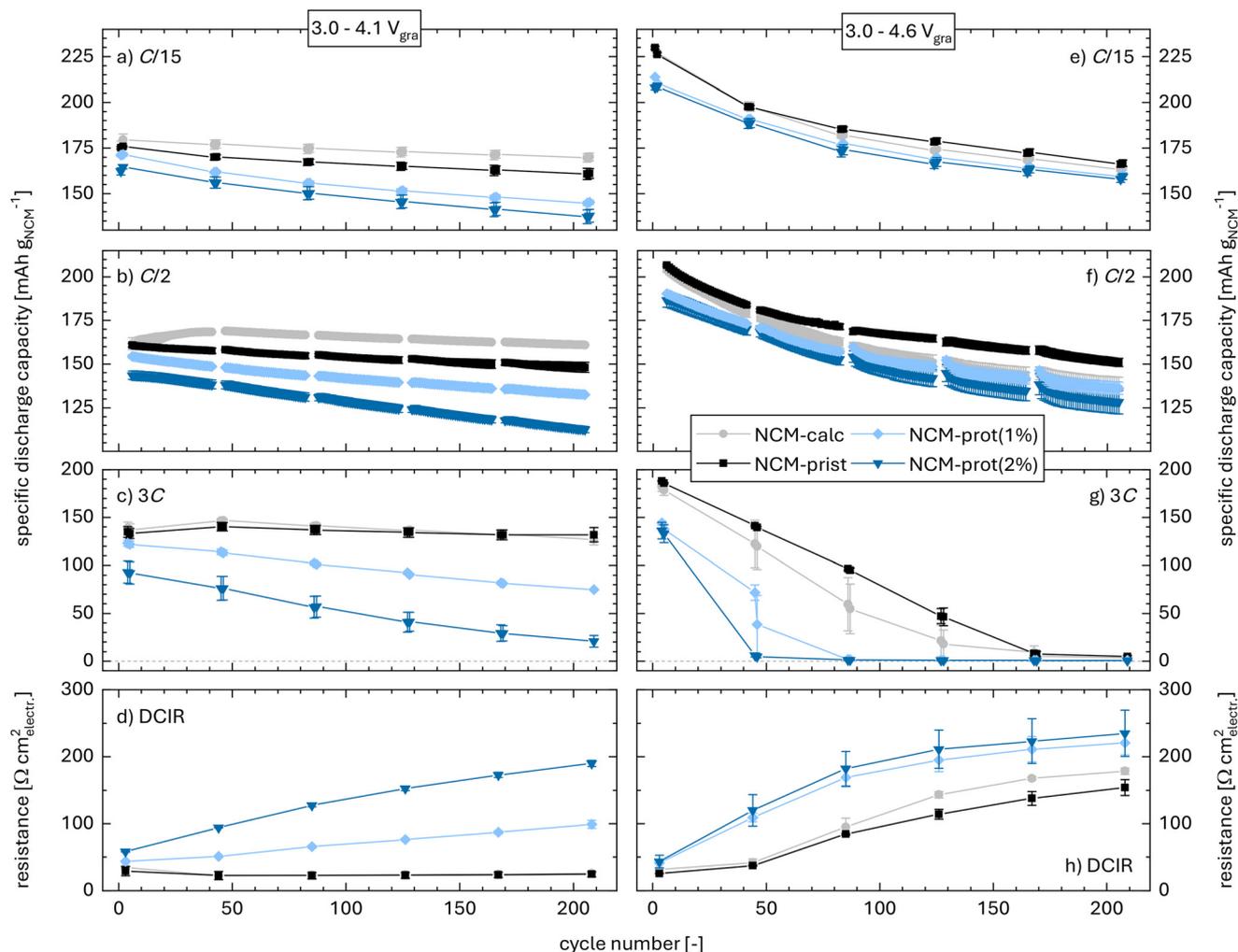
Fig. 5 Specific discharge capacities and DCIR values for the extended charge/discharge cycling test at 25 °C of NCM-calc (gray), NCM-prist (black), NCM-prot(1%) (light blue), and NCM-prot(2%) (dark blue) as WEs in coin full-cells, whereby the WE was cycled *vs.* a graphite CE with an N : P ratio of 1.1 : 1, with one Celgard H2013 separator and 30 μL LP57 electrolyte. One set of electrodes was cycled from 3.0–4.1 V_{gra} (a–d), while a second set was cycled from 3.0–4.6 V_{gra} (e–h). The applied *C*-rates were identical for all cells: two *C*/15 cycles (panels a and e) were followed by a half-cycle to 3.8 V_{gra} with *C*/15, where a 1 and 10 s DCIR pulse was measured with a current of *C*/2 (the 10 s pulse resistances are shown in panels d and h). The DCIR pulses were followed by two 3*C* cycles (b, f) and 36 *C*/2 cycles (c and g). All *C*-rates are based on a theoretical NCM capacity of 275 mAh g_{NCM}^{-1}. (a–c) & (e–g) specific discharge capacity as a function of cycle number; (d & h) 10 s DCIR resistance in Ω $cm^2_{electr.}$, *i.e.*, normalized to the geometrical area of the WE. All values are based on two nominally identical cells, and the error bars represent the minimum/maximum values.

particular at the end of charge) were kept below the onset potential of oxygen release and proton deintercalation to exclusively probe the effects of protons remaining in the active material. In the second set, the upper cutoff voltage was increased to 4.6 V_{gra} (or ~4.65 V_{Li}), where, as shown by OEMS (see Fig. 1), (i) O_2 evolution is observed for NCM-prist and NCM-calc, indicating the release of lattice oxygen (starting at $U \geq 4.3$ V_{Li}), and (ii) protons start to deintercalate from NCM-prot(2%) (starting at $U \geq 4.5$ V_{Li}). Here, it has to be noted, that only a fraction of the protons is expected to deintercalate during the first charge: when comparing the applied potential range with the OEMS results, then, at 4.6 V_{gra} (~4.65 V_{Li}), ~8% of the total evolved PF_5 is obtained for NCM-prot(1%), and ~25% for NCM-prot(2%). For better visibility, the discharge

capacities depicted in Fig. 5 are separated based on *C*-rates, with *C*/15 in panels a & e, *C*/2 in panels b & f, and 3*C* in panels c & g; the associated direct-current internal resistance (DCIR) of 10 s are shown in panels d & h.

When comparing the first cycles between 3.0 and 4.1 V_{gra} at *C*/15 (Fig. 5a), NCM-calc exhibits a discharge capacity of 174.9 mAh g_{NCM}^{-1} in the first cycle. The minor increase in the subsequent cycles is attributed to slight NCM particle cracking, by which more NCM surface area becomes accessible, enhancing the (de)lithiation kinetics.[58] Over 200 cycles, the capacity slightly decreases to 170.1 mAh g_{NCM}^{-1}, corresponding to a capacity retention of 97.2% at EOT. Compared to NCM-calc, NCM-prist delivers a similar initial discharge capacity of 175.1 mAh g_{NCM}^{-1} in the first cycle, as well as a

larger capacity fading, with a capacity retention of 92.0% at EOT (161.1 mAh g_{NCM}^{-1}). An even lower initial capacity as well as a higher capacity fade is visible for the protonated NCMs: NCM-prot(1%) provides 171.2 mAh g_{NCM}^{-1} in the first cycle, and 145.3 mAh g_{NCM}^{-1} at EOT, which corresponds to a capacity retention of only 84.9%. NCM-prot(2%) has an initial capacity of 162.1 mAh g_{NCM}^{-1}; at EOT, the capacity decreased to 137.9 mAh g_{NCM}^{-1}, corresponding to a capacity retention of 85.1%. These trends are also reflected at a higher C-rate, whereby the capacity fading is more pronounced at higher rates. At C/2 (Fig. 5b), the stark difference between protonated and non-protonated NCMs becomes even more evident, and while the NCM-calc fades with a rate of 0.05 mAh g_{NCM}^{-1} per cycle, the fading of NCM-prot(2%) is magnified to 0.15 mAh g_{NCM}^{-1} per cycle (comparing cycles 47 and 205), which is approximately a three-fold accelerated aging. At a higher C-rate. i.e., 3C (Fig. 5c), fading seems to progressively increase further. Fig. 5d shows the 10 s DCIR values (normalized to geometric cathode electrode area) that are calculated from a C/2 current pulse. NCM-calc and NCM-prist exhibit a slight decrease in resistance, namely from 34 and 29 Ω $cm^2_{electr.}$ to 26 and 24 Ω $cm^2_{electr.}$, respectively. In contrast, the first measured resistances (acquired after the first two C/15 cycles) are already higher for the protonated NCMs, which increase rapidly during cycling: for NCM-prot(1%), the DCIR increases by 128% from 43 Ω $cm^2_{electr.}$ at BOT to 99 Ω $cm^2_{electr.}$ at EOT, and, for NCM-prot(2%), the DCIR increases even by 228% from 58 to 190 Ω $cm^2_{electr.}$. Hence, the increase in the cell resistance scales with the proton content, resulting in a diminished rate capability for the protonated NCMs; the origin of this resistance build-up is assessed by the impedance analysis in Fig. 6.

For a second set of cells cycled to an upper cutoff voltage of 4.6 V_{gra} (see Fig. 5e–h), for which the OEMS data suggest that protons will be (at least partially) deintercalated from the NCM during cycling, the effect of the removal of protons on the capacity fading and the resistance build-up is examined. During the first two C/15 cycles (Fig. 5e), the initial discharge capacities cluster into two groups with similar performance: NCM-calc (229.3 mAh g_{NCM}^{-1}) and NCM-prist (229.9 mAh g_{NCM}^{-1}) show essentially the same capacity in their first cycle, as well as a similar capacity fading from BOT and EOT, namely 71.6% (to 164.1 mAh g_{NCM}^{-1}) and 72.5% (to 166.6 mAh g_{NCM}^{-1}), respectively. In comparison, less initial capacity is delivered by NCM-prot(1%) (213.7 mAh g_{NCM}^{-1}) and NCM-prot(2%) (208.0 mAh g_{NCM}^{-1}), yet showing an EOT capacity similar to the non-protonated materials, with 75.1% (160.5 mAh g_{NCM}^{-1}) and 76.6% (159.4 mAh g_{NCM}^{-1}), respectively. Very similar trends are observed at C/2 (Fig. 5f), and the differences in specific capacity of the four materials at EOT are only roughly half of those observed for the cells cycled to the lower cutoff voltage of 4.1 V_{gra} (see Fig. 5b). Interestingly, for both protonated samples, the capacity at C/2 seems to temporarily increase after the C/10-DCIR-3C sequence (i.e., at the beginning of each C/2 sequence); its origin remains unknown. At 3C (Fig. 5g), the same trends apply, and while the capacity fades faster for the protonated NCMs, while, at EOT, the measurable

capacity is below 5 mAh g_{NCM}^{-1} for all materials. When comparing these findings with the measured DCIR (Fig. 5h), it becomes obvious that both the initial and the final resistances are within a factor of ∼2 for the protonated (EOT: 220.7 and 234.9 Ω $cm^2_{electr.}$, for NCM-prot(1%) and NCM-prot(2%)) and the non-protonated (EOT: 154.0 and 178.5 Ω $cm^2_{electr.}$, for NCM-prist and NCM-calc) NCMs.

For the here examined upper cathode cutoff voltage of 4.6 V_{gra} (corresponding to ∼4.65 V_{Li}), the surface of non-protonated NCMs is known to reconstruct into a resistive rock-salt phase, driven by the release of lattice oxygen.[5,6] In the case of protonated NCMs cycled to above 4.5 V_{Li}, one would also expect the release of lattice oxygen, but via the formation of H_2O due to the absence of O_2 evolution, as observed by OEMS (Fig. 1), presumably leading to a similar oxygen-depleted surface phase. The resulting resistive surface layer, obtained both in the presence and the absence of protons, gives rise to the rather similar capacity fading and resistance growth of the protonated and non-protonated NCMs in Fig. 5e to h. On the other hand, for the lower cutoff voltage of 4.1 V_{gra}, no rocks-salt formation is expected, as the respective NCM potential of 4.15 V_{Li} is significantly below the onset of O_2 evolution at ∼4.3 V_{Li} (Fig. 1). However, the rapid DCIR increase of the protonated NCMs cycled to 4.1 V_{Li} does suggest the formation of a resistive oxygen-depleted surface layer, which seems to form already at such low potentials of up to 4.1 V_{gra}. The removal of oxygen may occur by the reaction of intercalated protons with lattice oxygen in the near-surface region of the NCM particles, analogously to the thermally-driven process given by eqn (7). To test this hypothesis, an experiment was conducted aiming to deintercalate the protons within two initial formation cycles by reaching an upper cutoff voltage of 4.6 V_{gra}, after which it was decreased to 4.1 V_{gra} for the subsequent cycles. However, as shown in Fig. S4, the high-voltage formation cycles did not reduce the capacity fading of the protonated NCM during extended cycling, which suggests that intercalated protons cannot be fully deintercalated within two cycles to 4.6 V_{gra}.

Further, as indicated before, a proton-induced $LiPF_6$-depletion could contribute to the deterioration of the electrochemical performance: assuming the release of all intercalated protons as H^+(eqn (5)), i.e., not in the form of H_2O, NCM-prot(2%) could deplete as much as 10% of the conductive salt (assuming a cathode loading of 10 mg_{CAM} cm^{-2} and 30 µL LP57 electrolyte, corresponding to ∼12 $g_{electrolyte}$/Ah for a practical capacity of 200 mAh g_{NCM}^{-1}). As shown by Hartmann et al.,[17] a depletion of the available $LiPF_6$ concentration may lead to a drastic reduction of the electrolyte conductivity and rate capability, with devastating consequences at high rates. As the amount of electrolyte per available capacity in large-format cells is typically lower by a factor of up to 10 compared to the values from this study,[59,60] the effect could even be more detrimental for commercial cells. However, the pronounced resistance build-up at 4.1 V_{gra} cannot be fully explained by the partial decomposition of the electrolyte salt, which will be further elucidated in the impedance analysis in Fig. 6 and is summarized in Scheme 1.

As eqn (5) indicates, the proton-driven decomposition of the $LiPF_6$ salt generates HF, which may induce an enhanced TM dissolution from the NCM. Hence, the impact of the protonation of the NCM on the TM dissolution is analyzed next.

Elemental analysis of cycled graphite anodes

It is believed that the dissolution of transition metals from layered-transition-metal–oxide CAMs can be caused by either HF,[61,62] that, as discussed above, is formed by the reaction of H_2O or protic species with $LiPF_6$,[46,63,64] and/or by protons that are formed upon the electrochemical oxidation of the electrolyte at high potentials.[51] Pronounced TM dissolution from the cathode and their subsequent deposition on the anode is reported to drive solid-electrolyte-interphase (SEI) layer growth, which results in accelerated impedance build-up, LLI, and gas evolution.[65–68] Though Jung et al.[22] concluded that, after ambient storage of Ni-rich NCMs, the formed surface impurities did not lead to TM dissolution, the effect of the presence of intercalated protons has not been considered. Therefore, graphite anodes were harvested after 200 cycles to 4.1 V_{gra} (see left panels of Fig. 5) and, to quantify the amount of deposited TMs, ICP-AES was conducted. Electrodes from this cutoff voltage were chosen to avoid the TM dissolution caused by the electrochemical electrolyte oxidation at higher potentials, which occurs at 25 °C at potentials above $\sim$4.65 V_{Li}.[51,69,70] Based on this, cycling the NCM-prot(2%) material to only 4.1 V_{gra} (or $\sim$4.15 V_{Li}) should reveal the extent of TM dissolution which stems from the protons in the NCM, while the analysis of cells with NCM-calc serves as a reference for an NCM material without any protons.

As shown in Table 1, the amount of TMs detected on the graphite anodes (in $\mu g\ cm^{-2}_{electr.}$) is up to 2-fold higher for the cells cycled with the NCM-calc material compared to those cycled with the NCM-prot(2%) material. When referencing the amount of TMs found in the graphite anodes to the amount of TM in the NCM (in units of $\mu mol_{TM}\ mol_{NCM}^{-1}$ or ppm, Table 1), it becomes apparent that only a relatively small fraction of the TMs in the NCM are dissolved over the 200 cycles between 3.0–4.1 V_{gra}; based on an estimate proposed by Oswald et al.,[32] the values obtained for the NCM-calc and NCM-prot(2%) material correspond to at most 45% and 32% of a monolayer of the NCM particles, which may simply be due to the dissolution of TM carbonate/hydroxide surface species. Interestingly, instead of the expected molar ratio of 83 : 12 : 05 of Ni : Co : Mn of the bulk NCM with more Co than Mn, the detected ratios of 87 : 04 : 08 and 80 : 04 : 15 expose a preferred dissolution of Mn over Co; however, if a significant amount of the detected TMs stems from surface contaminants, the observed values may indicate an increased concentration of Mn salts on the surface of the NCM, which are partially removed during washing.

Upon comparison of the results with literature, it becomes evident that, while for all these studies slightly different conditions were applied, the results of our study show good agreement with the ones from the literature, exhibiting dissolved amounts of typically less than a monolayer of NCM material,

Table 1 ICP-AES elemental analysis of graphite anodes harvested after more than 200 charge/discharge cycles between 3.0–4.1 V_{gra} from the coin cells with NCM-calc and NCM-prot(2%) from the experiments depicted in the left panels of Fig. 5. The amounts of TMs are referenced to the geometric area of the anode electrodes (in units of $\mu g\ cm^{-2}_{electr.}$), while the ppm values represent the amount of the TMs in the graphite anodes referenced to the amount of NCM in the cells ($\mu mol_{TM}\ mol_{NCM}^{-1}$). Note that the bulk composition of the NCM corresponds to a molar ratio of Ni : Co : Mn of 83 : 12 : 5. The given error is related to the standard deviation between a repeat ICP-AES measurement of the same sample. The last row indicates the calculated fraction of a monolayer (ML) that was dissolved from the cathode

| TM	NCM-calc		NCM-prot(2%)	
	$\mu g\ cm^{-2}_{electr.}$	ppm	$\mu g\ cm^{-2}_{electr.}$	ppm
Ni	2.27 ± 0.01	425 ± 1	1.35 ± 0.12	271 ± 24
Co	0.10 ± 0.01	19.3 ± 1.1	0.08 ± 0.00	15.3 ± 0.0
Mn	0.22 ± 0.01	43.7 ± 1.1	0.25 ± 0.02	54.6 ± 3.3
ML	45%		32%	

even when the cells were cycled at elevated temperatures of 45 °C.[42,71] Therefore, the presence of the protons in the NCM appears to not enhance TM dissolution. As a matter of fact, the lower TM dissolution observed for the NCM-prot(2%) CAM may be due to the removal of Ni-carbonate/-hydroxide surface species upon washing.[19,25,31] Hence, TM dissolution can be excluded as the underlying mechanism of the resistance build-up observed for the protonated NCM materials. Therefore, as a next step, the increased DCIR resistance is investigated in greater detail by performing electrochemical impedance spectroscopy.

Electrochemical impedance spectroscopy

To deconvolute the resistance into anode and cathode contributions, identical long-term experiments as the ones in coin full-cells up to 4.1 V_{gra} were repeated with T-cells, which were equipped with a lithiated gold-wire micro-reference electrode (GWRE),[41] whereby after each DCIR measurement, potentiomode electrochemical impedance spectroscopy (PEIS) was recorded at the same potential of 3.8 V_{gra} (corresponding to $\sim$3.9 V_{Li} or $\sim$50% SOC of the NCM, when referenced to its theoretical capacity). The results from the PEIS experiments are depicted as Nyquist plots in Fig. 6, where the top row panels (a–c) show the spectra of the cells with the different NCMs at BOT, and the bottom row panels (d–f) show the spectra at EOT (i.e., after 200 cycles between 3.0–4.1 V_{gra}). The left column of Fig. 6 shows the spectra of the cell with NCM-prist, the middle column those of the cell with NCM-prot(1%), and the right column those of the cells with NCM-prot(2%). In all spectra, the data point recorded at 1 Hz is marked with a circle to facilitate the comparison. A detailed discussion of the minor differences in the cycling behavior between coin and T-cells is given in the SI (Fig. S5).

Fig. 6a shows the impedance of the NCM-prist cell at BOT. Its full-cell impedance (gray line) is substantially smaller than that of the cells with the protonated NCMs (Fig. 6b and c).
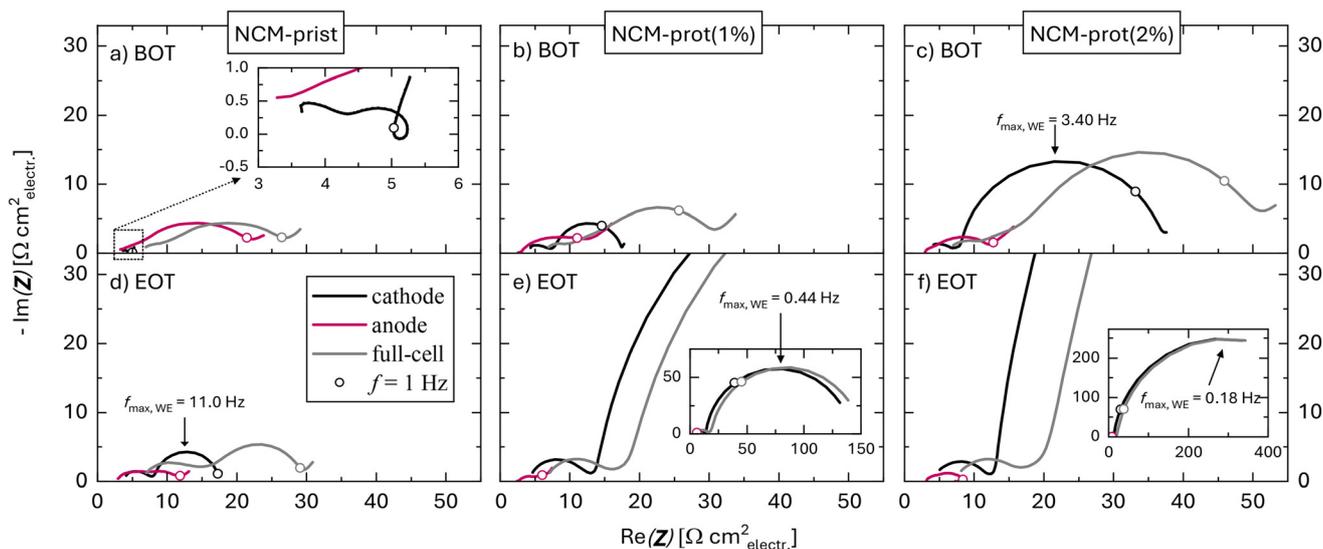
Fig. 6 Impedance spectroscopy in T-cells with gold-wire μ-RE, where a graphite CE was cycled at 25 °C *vs.* NCM-prist (a & c), NCM-prot(1%) (b & d), NCM-prot(2%) (c & f) as WEs (the cells contained two glass-fiber separators and 60 μL LP57 electrolyte). The cells were cycled in accordance with the coin full-cells between 3–4.1 V_{gra} (as shown in the left panels of Fig. 5), and after each 10 s DCIR pulse at 3.8 V_{gra}, the cells were connected to a different potentiostat, where impedance spectra were recorded at OCV (between 100 kHz and 100 mHz, with an amplitude of 15 mV). The upper panels (a–c) show the Nyquist plots after the two C/15 formation cycles and the DCIR pulse at BOT, and the bottom panels (d–f) show the EOT spectra after 208 cycles. Owing to the GWRE, the recorded full-cell impedance (WE-CE, gray lines) can be deconvoluted into cathode (WE-RE, black lines) and anode (CE-RE, pink lines) contributions. The impedance measured at a frequency of $f = 1$ Hz is marked by a circle, and, for the EOT spectra, the frequency at the maximum of the low-frequency semicircle is given as $f_{max, WE}$.

Furthermore, the full-cell impedance remains relatively constant until EOT for the cell with the NCM-prist material, while it increases drastically for the cells with the protonated NCMs, more so for the cell with NCM-prot(2%) (Fig. 6f) than for the one with NCM-prot(1%) (Fig. 6e).

In addition to the full-cell impedance ($Z_{full-cell}$), the anode impedances (Z_{CE}, pink lines) and the cathode impedances (Z_{WE}, black lines) are plotted. Since $Z_{WE} + Z_{CE} = Z_{full-cell}$, it becomes obvious that the main contribution to the full-cell impedance for the NCM-prist cell mostly stems from the anode; the cathode impedance is much smaller and is afflicted by an artefact, owing to the very high impedance of the GWRE in combination with the large difference between anode and cathode impedance.[41,72] Interestingly, for the NCM-prot(1%) (Fig. 6b) and the NCM-prot(2%) cells (Fig. 6c), the cathode dominates the full-cell impedance, while the contribution from the graphite anode is relatively small. In the literature, it has been suggested that the presence of water facilitates the formation of a possibly more conductive SEI, thus decreasing the anode impedance.[73,74] Hence, if part of the intercalated protons would be released as water already during the first few cycles, this could likely impact the anode impedance. Until EOT, the anode contribution is further reduced for all NCM materials, and the overall cell impedances are dominated by the contributions of the cathode.

All cathode spectra consist of two semicircles, one in the high-frequency region and one at lower frequencies, which can be fitted using a simple equivalent-circuit model, with the ionic resistance of the electrode being neglected in this simplified model, with a resistance (R) in series with two sets of a resistor and a constant-phase elements (Q) in parallel ($R_1-R_2/Q_2-R_3/Q_3$). Detailed results for the fittings are given in the SI (Fig. S6 and Table S1). Owing to the nature of the frequency response of the different types of resistances, they can be attributed to different processes in the cathode:[75,76] R_1 corresponds to the high-frequency resistance (R_{HF}) between the cathode and the GWRE located mid-cell, which stems mostly from the ionic resistance of the separator. R_2 that corresponds to the high-frequency semicircle represents the electrical contact resistance $R_{cont.}$ between the cathode current collector and the cathode electrode coating; it can increase over extended cycling due to poor adhesion, as well as due to the corrosion and passivation of the current collector by the reaction of Al_2O_3 with HF.[31,77,78] R_3, represented by the low-frequency semicircle, denotes mostly the charge-transfer resistance (R_{CT}) for the lithium (de)intercalation reaction, and is inversely proportional to the electrochemically active surface area of the active material. The resistance values resulting from the fit of the cathode impedances to this model are shown in Table S1. For the NCM-prist cathode, R_{HF} and $R_{cont.}$ values increase slightly from BOT to EOT, namely from 2.1 to 3.0 Ω cm$^2_{electr.}$, and from 2.6 to 5.3 Ω cm$^2_{electr.}$, respectively; the former indicates an increase of the separator resistance that might be caused by changed ionic conductivity and decomposition products of the proton-induced degradation of $LiPF_6$,[17] while the latter can be ascribed to current-collector corrosion and/or delamination of the cathode coating due to volume expansion during (de)lithiation and/or particle

cracking.[79–81] Since the relative contributions of R_{HF} and $R_{cont.}$ remain relatively small compared to the overall impedance of the cathode (especially at EOT), both separator resistance as well as contact resistance are not responsible for the significant increase in resistance of the protonated NCMs upon cycling, as discussed above for Fig. 5; thus, the electrolyte conductivity is not compromised significantly, and the previously mentioned effect of electrolyte-salt depletion does play a major role in the performance decline of the full-cells. Nonetheless, as resistances measured at very high frequencies can be prone to artifacts, a quantitative analysis is beyond the scope of this study.

The impedance spectra for the protonated NCMs also consist of two semicircles, and R_{HF} and $R_{cont.}$ increase in the same order of magnitude like NCM-prist (cf. Table S1, SI). R_{CT}, however, is already more pronounced at BOT, where 10.0 and 28.2 Ω cm$^2_{electr.}$ are recorded for NCM-prot(1%) (Fig. 6b) and NCM-prot(2%) (Fig. 6c), respectively. Considering the larger BET surface area of the protonated samples (Fig. S2), the actual resistance in the protonated CAM must be even more pronounced. An impaired solid-state lithium diffusion would also lead to a larger impedance, which would manifest as a Warburg element at low frequencies, superimposing with R_{CT}.[57] As this is occasionally erroneously interpreted, the Nyquist plot of NCM-prot(1%) is revisited. Here, nearly the entire semicircle is recorded (measured until 0.1 Hz), including the impedance approaching low imaginary-impedance values (i.e., close to the x-axis of the Nyquist plot) in the low-frequency region. In contrast, a true diffusion limitation prevents the semicircle trajectory beyond the apex from its decreasing trend and approaches a plateau extending into a characteristic diffusion tail at low frequencies (≈0.1 Hz). Hence, a diffusion limitation can be excluded (see additional discussion for Fig. S7). Surprisingly, at EOT, R_{CT} increases at least by an order of magnitude to 126.8 and 558.2 Ω cm$^2_{electr.}$ and dominates the impedance spectrum (NCM-prot(1%) in Fig. 6e and NCM-prot(2%) in Fig. 6f). This large increase is consistent with the increased DCIR in the full-cell experiments (Fig. 5); the discrepancy between the 10 s DCIR and R_{CT} is that parts of the semicircle lie outside the recorded frequency range, and R_{CT} stems from a fit, which extrapolates to lower frequencies. The 10 s pulse effectively probes the frequency range between ~0.1 and 0.01 Hz, where the impedance response of the protonated EOT electrodes is predominantly governed by the large cathode-side R_{CT}. Consequently, the resistance measured from the pulse primarily reflects the rise in R_{CT} within this regime, as discussed in more detail in Table S1. The severe aging/degradation of the CAM can result in an increase in R_{CT}, i.e., due to oxygen release or the formation of a resistive film from electrolyte decomposition products.[11,79,82] While it was not observed by OEMS that protons deintercalate at potentials below 4.5 V_{Li} (see Fig. 1), the similar resistance at EOT and the fact that the increased resistance originated from the cathode indicates the probable formation of a resistive near-surface layer within the NCM particles upon cycling.
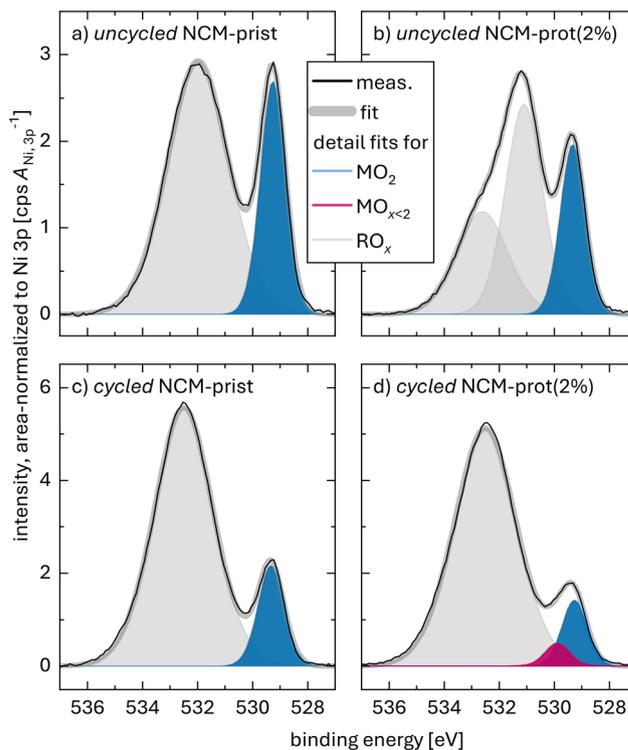

Fig. 7 X-ray photoelectron spectroscopy data for uncycled (a) NCM-prist, and (b) NCM-prot(2%) electrodes, and for cycled post-mortem electrodes, which were harvested from the coin full-cells at EOT, cycled at 25 °C between 3.0–4.1 V_{gra}, (Fig. 5): (c) NCM-prist, and (d) NCM-prot(2%). The O 1s core level in the binding-energy range between 537–527 eV is presented, and the counts are normalized to the area of the Ni 3p core level, and a Shirley background is subtracted. The measured counts are represented with a black line, the fit for MO$_2$ in blue, and MO$_{x<2}$ in pink. In light gray, fit(s) for a mixed oxygen-containing component (RO$_x$) are added, which constitutes oxygen in surface contaminants, binder, conductive carbon, and possibly degradation products on the electrode. All peaks are fitted using a GL(30) fit function. All spectra are binding-energy-corrected to the adventitious-carbon peak at 284.8 eV (data not shown).

Hence, a post-mortem investigation from harvested cathode electrodes after the long-term cycling experiment is appended. While an electrochemical analysis only revealed slight LAM (Fig. S8), the surface of the CAM is characterized by X-ray photoelectron spectroscopy (XPS) next.

X-ray photoelectron spectroscopy

The electrodes, which were cycled at 25 °C between 3.0–4.1 V_{Li} were harvested from the full-cells at EOT, and the spectra recorded by XPS are evaluated here. In Fig. 7, the oxygen O 1s spectra of uncycled and cycled NCM-prist and NCM-prot(2%), respectively, are shown in the binding energy (BE) range of 537.0–527.0 eV. In all spectra, the counts are normalized to the area of the Ni 3p core level ($A_{Ni\ 3p}$, Fig. S9) from the respective measurement to improve the comparability since the oxygen intensity is now referenced to the nickel in the NCM. All BE positions and the full width at half maximum (FWHM) are also summarized in Table S2 in the SI.
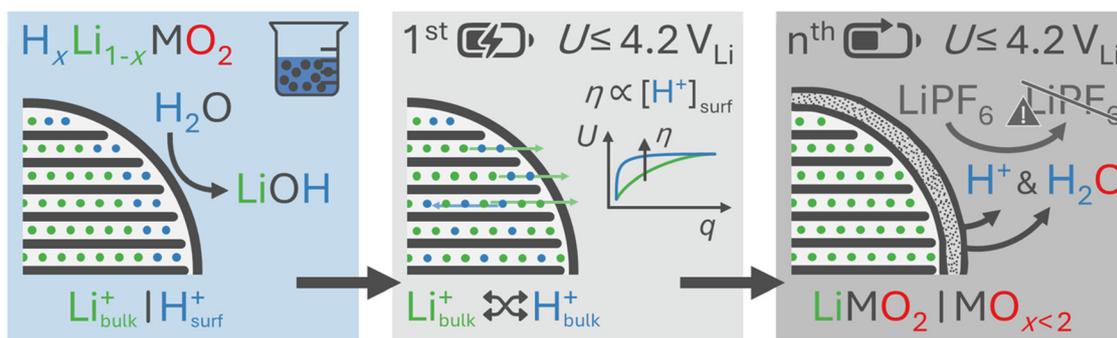
Scheme 1 Graphical summary of the key findings of this work. The as-received NCM is washed with H_2O (left panel), resulting in a phase-separated, protonated surface layer and a lithiated bulk ($H_xLi_{1-x}MO_2$). During the first charge/delithiation (middle panel), lithium has to pass through the protonated layer, leading to an increased overpotential at low SOCs. After having reached a sufficient degree of delithiation, the protons and the lithium mix homogeneously. After cycling to either a potential or for extended cycling to lower potentials (right panel), protons are released as protons and water, accompanied by the formation of a resistive, oxygen-depleted $MO_{x<2}$ phase at the surface of the NCM particles, leading to the decomposition of conductive salt in the electrolyte.

As shown in Fig. 7a, uncycled NCM-prist electrode exhibits two well separated peaks, where one is located at lower BEs at 529.3 eV with a FWHM of 1.1 eV. This species is assigned to the oxygen in the layered MO_2 phase.[10,83,84] The second peak is shifted to higher BEs by 2.7 eV to 532.0 eV, and is attributed to surface contaminants, such as LiOH and Li_2CO_3, as well as oxygen in the conductive carbon.[84–88] Here, only one peak is fitted, yet the very broad FWHM of more than 2 eV implies that it consists of several species contributing to this peak. Since a rigorous deconvolution of these species is beyond the scope of this work, all species are summarized as "RO_x". In Fig. 7b, MO_2 can again be attributed to the peak at 529.3 eV and a FWHM of 1.1 eV. The findings of our previous study[32] have shown that the NCM lattice remains layered regardless of whether Li^+ or H^+ are intercalated; this is now confirmed, as in this XPS spectrum from the prepared and dried electrodes, only one peak shows for MO_2 and no signs of oxygen depletion are detected. At higher BEs, a slightly different shape of the curves allows two features to be fitted, at 531.1 eV (1.6 eV), and at 532.6 eV (2.2 eV), respectively, which could correspond to LiOH, typically found at a BE of 531.1 eV,[85,88] and Li_2CO_3, located at 532.4 eV.[84] The inherent difference between NCM-prist and NCM-prot(2%) is that, for the latter, carbonate-based surface contaminants have dissolved during the washing process, resulting in a smaller carbonate concentration at the surface.[32] Hence, for NCM-prot(2%), the surface composition and species differ from the NCM-prist, and hydroxides and carbonates can be differentiated.

In Fig. 7c, the O 1s core level from the harvested, cycled NCM-prist electrode is depicted. Again, this spectrum consists of two well separated peaks, and the one, which was previously assigned to the layered MO_2 phase, is still found at the same BE of 529.3 eV, with the same FWHM of 1.1 eV. The other peak has shifted slightly to higher BEs at 532.5 eV, with a FWHM of 2.5 eV, and its intensity has increased roughly by a factor of two. Since the electrodes were harvested after extended cycling, it is not surprising that the

amount of surface species has increased: in addition to the previously mentioned contaminants, likely electrolyte degradation products and/or residual salts, which were not washed away, are now also present on the surface of the NCM. The increased amount of surface species attenuates the MO_2 signal of the underlying NCM to a higher extent, and therefore the intensity of the MO_2 signal is slightly decreased in comparison to the uncycled electrode. In contrast to that, cycled NCM-prot(2%) (Fig. 7d) has an additional shoulder at 529.9 eV, which cannot be fitted without adding another component with a FWHM of 1.1 eV; by adding the additional species, the MO_2 peak remains unchanged at 529.3 eV with a FWHM of 1.1 eV. This additional species can be assigned to the formation of a $MO_{x<2}$ phase, for which BE and FWHM match nicely with literature.[83,84,89,90]

Therefore, the increase in R_{CT} of the protonated NCMs (Fig. 5 and 6), responsible for their diminished capacity retention, is attributed to the formation of an oxygen-depleted surface layer forming upon cycling, arising even for a cutoff potential below the onset of the release of protons or oxygen. While the upper cutoff voltage of 4.1 V_{gra} is lower than the expected potential onset for the oxygen release, it seems that the protons indeed deintercalate during extended charge/discharge cycling. We hypothesize that intercalated protons leave the NCM during repeated charge/discharge cycling through the reaction with lattice oxygen and the release as H_2O from the possibly unstable HMO_2 phase. This removal of oxygen results in the formation of a resistive oxygen-depleted surface layer which affects the performance in half- and full-cells negatively. As this seems to occur at potential below the electrochemical deintercalation of protons at 4.5 V_{Li}, this decomposition could stem from the repeated (de)intercalation of lithium or as a function of time (cf. visual summary in Scheme 1, right panel). The rate and the extent of the protons leaving the NCM host structure during electrochemical operation of the battery needs to be the scope of future studies.

Conclusions

Washing as well as improper handling and storage of Ni-rich NCMs introduce protons into the near-surface regions of the particles. This study quantifies the detrimental impact of 1 and 2 mol% of intercalated protons on the electrochemical performance of the NCM and reveals a previously unknown degradation mechanism driven by the present protons.

The electrochemical characterization in half-cells showed that, during the first charge, the protonated surface layer impedes lithium deintercalation, causing a diffusion overpotential of 200 mV for only 2 mol% of protons, even at very low C-rates (C/50). This effect fades after the first cycle due to a redistribution of the protons within the NCM particle. Furthermore, OEMS experiments exposed that protons deintercalate electrochemically at voltages above 4.5 V_{Li}. Further, a change in the oxygen release at high potential suggests that some protons might partially deintercalate in the form of water, leading to an oxygen-depleted surface layer. The released protons then decompose the $LiPF_6$ salt, reducing the electrolyte conductivity and evolving gaseous products, which were detected using OEMS.

Long-term cycling in full-cells revealed that, under mild conditions up to 4.1 V_{gra}, only non-protonated NCMs exhibit a stable cycling performance. In contrast, protonated materials suffer a three-fold accelerated capacity fading at a practically relevant C-rate of C/2, and severe impedance growth. By impedance spectroscopy using a μ-RE, a 20-fold increase of the charge-transfer resistance was detected for the protonated NCMs after 200 cycles to 4.1 V_{gra}, which was attributed to the formation of an oxygen-depleted surface layer, as confirmed by post-mortem XPS. While protonated NCMs do not enhance the transition-metal deposition on the anode, it was confirmed that the protons cause an inherently less stable NCM structure. These observations are summarized in Scheme 1.

Protons remaining in nickel-rich NCMs after washing or exposure to moisture have a devastating impact on the electrochemical performance, even under mild cycling conditions, and even for relatively small proton amounts of about 1 mol%. Furthermore, the detected difference in lifetime between NCM-calc and NCM-prist reveals that commercially available materials might already degrade during shipping or storage. The results from this study reveal a novel, proton-driven degradation mechanism, and consequently, contact between NCMs and water, whether through post-synthesis washing, storage, or electrode fabrication, should be minimized, if not avoided completely. This can be achieved by avoiding the use of an excess of lithium salt during synthesis, which could make the subsequent washing step obsolete, as well as by a sensible choice for a moisture level if the samples are handled in air.

If contact with water or moisture cannot be avoided, restoring the NCM structure after exposure to water is straightforward after ambient storage, while, after washing, a more rigorous approach is required: (1) When NCMs are stored in the presence of moisture, protons intercalate into the NCM structure but all lithium ions remain as surface contaminants on the material; thus, a re-calcination at typically 450 to 650 °C in dry, oxygen-containing atmosphere is expected to restore the NCM structure with the correct lithium-to-transition-metal stoichiometry. (2) In contrast, during washing, protons intercalate while the lithium ions are removed from the material by the washing solution; in this case, to restore the NCM structure fully without off-stoichiometry, the proton content has to be quantified, before the material is mixed with the corresponding amount of lithium salt to compensate for the removed lithium inventory and finally re-calcined. To ensure optimal electrochemical performance, both the absence of protons as well as the structural integrity of the NCM material are required.

Author contributions

Rebecca Wilhelm: conceptualization, data curation, formal analysis, investigation, methodology, visualization, writing – original draft. Simon Helmer: formal analysis, writing – review & editing. Hubert A. Gasteiger: conceptualization, funding acquisition, methodology, resources, writing – review & editing. Stefan Oswald: conceptualization, data curation, formal analysis, funding acquisition, investigation, methodology, writing – original draft.

Conflicts of interest

All authors declare that they have no conflicts of interest.

Data availability

Data for this article are available at Harvard Dataverse at https://doi.org/10.7910/DVN/ZNP4BO.

Supplementary information (SI): X-ray photoelectron spectra, scanning electron microscopy images, cycling data, and electrochemical impedance results. See DOI: https://doi.org/10.1039/d5eb00190k.

Acknowledgements

References

1 H.-J. Noh, S. Youn, C. S. Yoon and Y. K. Sun, *J. Power Sources*, 2013, **233**, 121.

2 M. H. Kim, H. S. Shin, D. Shin and Y. K. Sun, *J. Power Sources*, 2006, **159**, 1328.

3 W. Li, E. M. Erickson and A. Manthiram, *Nat. Energy*, 2020, **5**, 26.

4 U.-H. Kim, D.-W. Jun, K.-J. Park, Q. Zhang, P. Kaghazchi, D. Aurbach, D. T. Major, G. Goobes, M. Dixit, N. Leifer, C. M. Wang, P. Yan, D. Ahn, K.-H. Kim, C. S. Yoon and Y.-K. Sun, *Energy Environ. Sci.*, 2018, **11**, 1271.

5 R. Jung, M. Metzger, F. Maglia, C. Stinner and H. A. Gasteiger, *J. Electrochem. Soc.*, 2017, **164**, A1361.

6 S. Oswald and H. A. Gasteiger, *J. Electrochem. Soc.*, 2023, **170**, 030506.

7 J. Choi and A. Manthiram, *J. Electrochem. Soc.*, 2005, **152**, A1714.

8 A. O. Kondrakov, H. Geßwein, K. Galdina, L. De Biasi, V. Meded, E. O. Filatova, G. Schumacher, W. Wenzel, P. Hartmann, T. Brezesinski and J. Janek, *J. Phys. Chem. C*, 2017, **121**, 24381.

9 H. Li, A. Liu, N. Zhang, Y. Wang, S. Yin, H. Wu and J. R. Dahn, *Chem. Mater.*, 2019, **31**, 7574.

10 F. Friedrich, B. Strehle, A. T. S. Freiberg, K. Kleiner, S. J. Day, C. Erk, M. Piana and H. A. Gasteiger, *J. Electrochem. Soc.*, 2019, **166**, A3760.

11 B. Strehle, F. Friedrich and H. A. Gasteiger, *J. Electrochem. Soc.*, 2021, **168**, 050512.

12 R. Jung, P. Strobl, F. Maglia, C. Stinner and H. A. Gasteiger, *J. Electrochem. Soc.*, 2018, **165**, A2869.

13 J. Wandt, A. T. S. Freiberg, A. Ogrodnik and H. A. Gasteiger, *Mater. Today*, 2018, **21**, 825.

14 A. T. S. Freiberg, M. K. Roos, J. Wandt, R. De Vivie-Riedle and H. A. Gasteiger, *J. Phys. Chem. A*, 2018, **122**, 8828.

15 B. L. D. Rinkel, D. S. Hall, I. Temprano and C. P. Grey, *J. Am. Chem. Soc.*, 2020, **142**, 15058.

16 W. M. Dose, I. Temprano, J. P. Allen, E. Björklund, C. A. O'Keefe, W. Li, B. L. Mehdi, R. S. Weatherup, M. F. L. De Volder and C. P. Grey, *ACS Appl. Mater. Interfaces*, 2022, **14**, 13206.

17 L. Hartmann, L. Reuter, L. Wallisch, A. Beiersdorfer, A. Adam, D. Goldbach, T. Teufl, P. Lamp, H. A. Gasteiger and J. Wandt, *J. Electrochem. Soc.*, 2024, **171**, 060506.

18 W. Li, W. R. McKinnon and J. R. Dahn, *J. Electrochem. Soc.*, 1994, **141**, 2310.

19 J. Sicklinger, M. Metzger, H. Beyer, D. Pritzl and H. A. Gasteiger, *J. Electrochem. Soc.*, 2019, **166**, A2322.

20 J. Xiao, F. Shi, T. Glossmann, C. Burnett and Z. Liu, *Nat. Energy*, 2023, **8**, 329.

21 J. Kim, H. Lee, H. Cha, M. Yoon, M. Park and J. Cho, *Adv. Energy Mater.*, 2018, **8**, 1702028.

22 R. Jung, R. Morasch, P. Karayaylali, K. Phillips, F. Maglia, C. Stinner, Y. Shao-Horn and H. A. Gasteiger, *J. Electrochem. Soc.*, 2018, **165**, A132.

23 N. V. Faenza, L. Bruce, Z. W. Lebens-Higgins, I. Plitz, N. Pereira, L. F. J. Piper and G. G. Amatucci, *J. Electrochem. Soc.*, 2017, **164**, A3727.

24 A. C. Martinez, S. Grugeon, D. Cailleu, M. Courty, P. Tran-Van, B. Delobel and S. Laruelle, *J. Power Sources*, 2020, **468**, 228204.

25 L. Hartmann, D. Pritzl, H. Beyer and H. A. Gasteiger, *J. Electrochem. Soc.*, 2021, **168**, 070507.

26 S. E. Renfrew and B. D. McCloskey, *J. Am. Chem. Soc.*, 2017, **139**, 17853.

27 A. T. S. Freiberg, J. Sicklinger, S. Solchenbach and H. A. Gasteiger, *Electrochim. Acta*, 2020, **346**, 136271.

28 M. Metzger, B. Strehle, S. Solchenbach and H. A. Gasteiger, *J. Electrochem. Soc.*, 2016, **163**, A1219.

29 Z. Chen, J. Wang, J. Huang, T. Fu, G. Sun, S. Lai, R. Zhou, K. Li and J. Zhao, *J. Power Sources*, 2017, **363**, 168.

30 I. A. Shkrob, J. A. Gilbert, P. J. Phillips, R. Klie, R. T. Haasch, J. Bareño and D. P. Abraham, *J. Electrochem. Soc.*, 2017, **164**, A1489.

31 D. Pritzl, T. Teufl, A. T. S. Freiberg, B. Strehle, J. Sicklinger, H. Sommer, P. Hartmann and H. A. Gasteiger, *J. Electrochem. Soc.*, 2019, **166**, A4056.

32 S. Oswald, R. Wilhelm, T. Kratky, L. Szentmiklósi, B. Maróti, I. Harsányi, S. A. Hallweger, G. Kieslich, S. Günther and H. A. Gasteiger, *J. Mater. Chem. A*, 2024, **12**, 25140.

33 P. Xu, X. Guo, B. Jiao, J. Chen, M. Zhang, H. Liu, X. Yu, M. Appleberry, Z. Yang, H. Gao, F. Yang, X. Weng, Y. Shen, J. Gu, Y. S. Meng, C. Brooks, S. P. Ong and Z. Chen, *Nat. Commun.*, 2024, **15**, 9842.

34 T. Toma, R. Maezono and K. Hongo, *ACS Appl. Energy Mater.*, 2020, **3**, 4078.

35 M. Hofmann, M. Kapuschinski, U. Guntow and G. A. Giffin, *J. Electrochem. Soc.*, 2020, **167**, 140512.

36 Y. Zhou, Z. Hu, Y. Huang, Y. Wu and Z. Hong, *J. Alloys Compd.*, 2021, **888**, 161584.

37 Y. Kato, A. Nagahara, N. Gerile, S. Fujinaka, N. Hamamoto, H. Nishimura and H. Nakai, *J. Electrochem. Soc.*, 2022, **169**, 060543.

38 J.-H. Park, B. Choi, Y.-S. Kang, S. Y. Park, D. J. Yun, I. Park, J. H. Shim, J.-H. Park, H. N. Han and K. Park, *Energy Technol.*, 2018, **6**, 1361.

39 M. Bianchini, M. Roca-Ayats, P. Hartmann, T. Brezesinski and J. Janek, *Angew. Chem., Int. Ed.*, 2019, **58**, 10434.

40 N. Tsiouvaras, S. Meini, I. Buchberger and H. A. Gasteiger, *J. Electrochem. Soc.*, 2013, **160**, A471.

41 S. Solchenbach, D. Pritzl, E. J. Y. Kong, J. Landesfeind and H. A. Gasteiger, *J. Electrochem. Soc.*, 2016, **163**, A2265.

42 S. Oswald, M. Bock and H. A. Gasteiger, *J. Electrochem. Soc.*, 2023, **170**, 090505.

43 S. Oswald, D. Pritzl, M. Wetjen and H. A. Gasteiger, *J. Electrochem. Soc.*, 2021, **168**, 120501.

44 S. Oswald, M. Bock and H. A. Gasteiger, *J. Electrochem. Soc.*, 2022, **169**, 050501.

45 L. De Biasi, A. O. Kondrakov, H. Geßwein, T. Brezesinski, P. Hartmann and J. Janek, *J. Phys. Chem. C*, 2017, **121**, 26163.

46 S. Solchenbach, M. Metzger, M. Egawa, H. Beyer and H. A. Gasteiger, *J. Electrochem. Soc.*, 2018, **165**, A3022.

47 M. Stich, M. Göttlinger, M. Kurniawan, U. Schmidt and A. Bund, *J. Phys. Chem. C*, 2018, **122**, 8836.

48 K. Tasaki, K. Kanda, S. Nakamura and M. Ue, *J. Electrochem. Soc.*, 2003, **150**, A1628.

49 B. L. D. Rinkel, J. P. Vivek, N. Garcia-Araez and C. P. Grey, *Energy Environ. Sci.*, 2022, **15**, 3416.

50 R. Jung, M. Metzger, F. Maglia, C. Stinner and H. A. Gasteiger, *J. Phys. Chem. Lett.*, 2017, **8**, 4820.

51 L. J. Reinschlüssel, L. Reuter, P. Rapp, M. Bock, A. Berger, M. A. Schilling and H. A. Gasteiger, *J. Electrochem. Soc.*, 2025, **172**, 060536.

52 M. Metzger, P. Walke, S. Solchenbach, G. Salitra, D. Aurbach and H. A. Gasteiger, *J. Electrochem. Soc.*, 2020, **167**, 160522.

53 R. A. Huggins, *Energy Storage*, 2010.

54 R. Wilhelm, R. Schuster, T. Kutsch, S. Qian, J. Mahl, T. Kratky, J. Wandt, E. J. Crumlin and H. A. Gasteiger, *ACS Appl. Mater. Interfaces*, 2025, **17**, 38571.

55 G. Wan, T. P. Pollard, L. Ma, M. A. Schroeder, C.-C. Chen, Z. Zhu, Z. Zhang, C.-J. Sun, J. Cai, H. L. Thaman, A. Vailionis, H. Li, S. Kelly, Z. Feng, J. Franklin, S. P. Harvey, Y. Zhang, Y. Du, Z. Chen, C. J. Tassone, H.-G. Steinrück, K. Xu, O. Borodin and M. F. Toney, *Science*, 2024, **385**, 1230.

56 P. Kurzhals, F. Riewald, M. Bianchini, H. Sommer, H. A. Gasteiger and J. Janek, *J. Electrochem. Soc.*, 2021, **168**, 110518.

57 R. Morasch, H. A. Gasteiger and B. Suthar, *J. Electrochem. Soc.*, 2023, **170**, 080522.

58 R. Ruess, S. Schweidler, H. Hemmelmann, G. Conforto, A. Bielefeld, D. A. Weber, J. Sann, M. T. Elm and J. Janek, *J. Electrochem. Soc.*, 2020, **167**, 100532.

59 S. Solchenbach, C. Tacconis, A. Gomez Martin, V. Peters, L. Wallisch, A. Stanke, J. Hofer, D. Renz, B. Lewerich, G. Bauer, M. Wichmann, D. Goldbach, A. Adam, M. Spielbauer, P. Lamp and J. Wandt, *Energy Environ. Sci.*, 2024, **17**, 7294.

60 X. Wu, K. Pan, M. Jia, Y. Ren, H. He, L. Zhang and S. Zhang, *Green Energy Environ.*, 2019, **4**, 360.

61 J. Lüchtefeld, H. Hemmelmann, S. Wachs, K. J. Mayrhofer, M. T. Elm and B. B. Berkes, *J. Phys. Chem. C*, 2022, **126**, 17204.

62 R. Sahore, D. C. O'Hanlon, A. Tornheim, C.-W. Lee, J. C. Garcia, H. Iddir, M. Balasubramanian and I. Bloom, *J. Electrochem. Soc.*, 2020, **167**, 020513.

63 D. Strmcnik, I. E. Castelli, J. G. Connell, D. Haering, M. Zorko, P. Martins, P. P. Lopes, B. Genorio, T. Østergaard, H. A. Gasteiger, F. Maglia, B. K. Antonopoulos, V. R. Stamenkovic, J. Rossmeisl and N. M. Markovic, *Nat. Catal.*, 2018, **1**, 255.

64 C. L. Campion, W. Li and B. L. Lucht, *J. Electrochem. Soc.*, 2005, **152**, A2327.

65 N. P. W. Pieczonka, Z. Liu, P. Lu, K. L. Olson, J. Moote, B. R. Powell and J.-H. Kim, *J. Phys. Chem. C*, 2013, **117**, 15947.

66 T. Joshi, K. Eom, G. Yushin and T. F. Fuller, *J. Electrochem. Soc.*, 2014, **161**, A1915.

67 H. Zheng, Q. Sun, G. Liu, X. Song and V. S. Battaglia, *J. Power Sources*, 2012, **207**, 134.

68 K. Amine, Z. Chen, Z. Zhang, J. Liu, W. Lu, Y. Qin, J. Lu, L. Curtis and Y.-K. Sun, *J. Mater. Chem.*, 2011, **21**, 17754.

69 R. Jung, F. Linsenmann, R. Thomas, J. Wandt, S. Solchenbach, F. Maglia, C. Stinner, M. Tromp and H. A. Gasteiger, *J. Electrochem. Soc.*, 2019, **166**, A378.

70 L. Reuter, L. J. Reinschlüssel and H. A. Gasteiger, *J. Electrochem. Soc.*, 2024, **171**, 100524.

71 Z. Ruff, C. Xu and C. P. Grey, *J. Electrochem. Soc.*, 2021, **168**, 060518.

72 R. Morasch, B. Suthar and H. A. Gasteiger, *J. Electrochem. Soc.*, 2020, **167**, 100540.

73 U. Langklotz, M. Schneider and A. Michaelis, *J. Ceram. Sci. Technol.*, 2013, **4**, 69.

74 F. Huttner, W. Haselrieder and A. Kwade, *Energy Technol.*, 2020, **8**, 1900245.

75 J. Landesfeind, D. Pritzl and H. A. Gasteiger, *J. Electrochem. Soc.*, 2017, **164**, A1773.

76 M. Gaberscek, J. Moskon, B. Erjavec, R. Dominko and J. Jamnik, *Electrochem. Solid-State Lett.*, 2008, **11**, A170.

77 M. Wang, M. Tang, S. Chen, H. Ci, K. Wang, L. Shi, L. Lin, H. Ren, J. Shan, P. Gao, Z. Liu and H. Peng, *Adv. Mater.*, 2017, **29**, 1703882.

78 X. Zhang and T. M. Devine, *J. Electrochem. Soc.*, 2006, **153**, B375.

79 S. Schweidler, L. De Biasi, G. Garcia, A. Mazilkin, P. Hartmann, T. Brezesinski and J. Janek, *ACS Appl. Energy Mater.*, 2019, **2**, 7375.

80 S. Schweidler, L. De Biasi, P. Hartmann, T. Brezesinski and J. Janek, *ACS Appl. Energy Mater.*, 2020, **3**, 2821.

81 D. Pritzl, A. E. Bumberger, M. Wetjen, J. Landesfeind, S. Solchenbach and H. A. Gasteiger, *J. Electrochem. Soc.*, 2019, **166**, A582.

82 J. Li, J. Huang, X. Kong, J. Zeng and J. Zhao, *J. Power Sources*, 2021, **496**, 229856.

83 W. Li, X. Liu, Q. Xie, Y. You, M. Chi and A. Manthiram, *Chem. Mater.*, 2020, **32**, 7796.

84 A. T. S. Freiberg, S. Qian, J. Wandt, H. A. Gasteiger and E. J. Crumlin, *ACS Appl. Mater. Interfaces*, 2023, **15**, 4743.

85 A. C. Kozen, A. J. Pearse, C.-F. Lin, M. A. Schroeder, M. Noked, S. B. Lee and G. W. Rubloff, *J. Phys. Chem. C*, 2014, **118**, 27749.

86 S. Oswald, *Appl. Surf. Sci.*, 2015, **351**, 492.

87 A. Guéguen, P. Novák and E. J. Berg, *J. Electrochem. Soc.*, 2016, **163**, A2545.

88 W. Chia-Ching and Y. Cheng-Fu, *Nanoscale Res. Lett.*, 2013, **8**, 33.

89 A. N. Mansour, *Surf. Sci. Spectra*, 1994, **3**, 279.

90 A. N. Mansour, *Surf. Sci. Spectra*, 1994, **3**, 231.